Sustainable Energy & Fuels

Accepted Manuscript

Sustainable Energy & Fuels

Interdisciplinary research for the development of sustainable energy technologies

rsc.li/sustainable-energy

ROYAL SOCIETY OF CHEMISTRY

PAPER
Chengxiang Xiang, Nathan S. Lewis et al.
Evaluation of flow schemes for near-neutral pH electrolytes in solar-fuel generators

ROYAL SOCIETY OF CHEMISTRY

rsc.li/sustainable-energy

ARTICLE

Design of nanostructured 2D (photo-)electrocatalysts for biomass valorization coupled with H₂ production

Bahareh Feizi Mohazzab,*[a] Kiarash Torabi,[b] and Dandan Gao*[a]

Electrocatalytic water splitting driven by renewable energy is a promising strategy for sustainable hydrogen production. However, the slow oxygen evolution reaction (OER) kinetics severely limit the rate of the hydrogen evolution reaction (HER) and the overall energy conversion efficiency of the water electrolyzer. To overcome this challenge, hybrid water electrolysis systems have been developed which replace the sluggish OER with thermodynamically and kinetically favorable biomass (photo-)electro-oxidation. In addition, these systems allow for the simultaneous production of value-added chemical products. This review highlights the design strategies involving the host structure remodeling and structure assembly design of two-dimensional (2D) nanomaterial-based (photo-)electrocatalysts, as well as their wide application in hybrid water electrolysis. Moreover, the current challenges and emerging strategies for the development of advanced (photo-)electrocatalysts and industrial-scale systems are emphasized.

1. Introduction

Growing global energy demands and environmental crises have prompted researchers to explore cleaner and more sustainable energy technologies. In this regard, hydrogen (H₂) has been considered as an attractive energy carrier with high gravimetric energy density. In particular, H₂ can be produced in a carbon-neutral fashion and a sustainable energy scheme can be built to this end.[1, 2] For example, electrochemical (EC)[3,4-6] or photoelectrochemical (PEC)[7-9] water splitting have been widely employed for green H₂ production. However, the sluggish oxygen evolution reaction (OER) with proton-coupled four-electron transfer process is currently the main bottleneck, requiring high voltage supply (>1.8 V vs. RHE),[10] suffering from instability of applied catalyst during operation (e.g., benchmark IrO₂ OER catalyst degradation under harsh alkaline or acidic conditions[11, 12]), and thus preventing large-scale industrial deployment. In consequence, conventional water splitting for efficient H₂ production with economic and ecological viability remains a challenge.[13, 14]

One approach to overcome this challenge is hybrid water electrolysis. In this context, hydrogen evolution reaction (HER) can be alternatively coupled with industrially important (photo-)electro-oxidation reactions, which can produce high-value products while requiring lower overpotentials as compared to the OER. Over the last decade, this novel concept has thrived, and led to major breakthroughs for (photo-)electro-oxidation of organics, including alcohols,[15, 16] aldehydes,[17, 18] carboxylic acids,[19, 20] amines,[21, 22] ammonia,[23, 24] and hydrazine.[25, 26] In addition, biomass feedstocks valorization is one of the most attractive (photo-)electro-oxidation reactions.[27, 28] For example, 5-hydroxymethyl furfural (HMF), which possesses different functional groups such as furan ring, aldehyde group, and hydroxymethyl group, can also be valorized to chemicals and fuels with higher values (details see Electronic Supplementary Information (ESI), **Figure S1a**). In this regard, furandicarboxylic acid (FDCA) is one of the desired products, which is an important alternative to petroleum-derived terephthalic acid in polymer industry.[29] Moreover, glucose is considered as another ideal biomass feedstock, which is a waste product generated in the pulp and paper processing industry.[30] For this reason, glucose oxidation is emerging as an industrially important valorization strategy for value-added products, such as gluconic acid (GLA), glucaric acid (GUA), formic acid (FA), tartaric acid and glycolic acid (ESI, **Figure S1b**). For another example, lignin, as one of the most abundant biomass, can be converted into value-added products through photocatalysis, EC and PEC under oxidative conditions.[31] During the oxidation process, functional groups and chemical bonds of lignin can be oxidized through different pathways, including side-chain linkages, aromatic rings, and phenolic hydroxyl groups (ESI, **Figure S2**).[32] Altogether, to give an overview of the biomass and its valorization involved in this review, a summary table is included in the ESI (**Table S1**)

The establishment of sustainable systems for simultaneous H₂ production and biomass valorization requires the exploration of low-cost and robust (photo-)electrocatalysts with high performance, including superior intrinsic catalytic activity, excellent selectivity and outstanding durability.[33, 34] In this context, two-dimensional (2D) nanomaterials have become an attractive class of (photo-)electrocatalysts which combine a variety of desirable properties

[a.] *Department of Chemistry, Johannes Gutenberg University Mainz, Duesbergweg 10-14, 55128 Mainz, Germany*
Emails: bahareh.feizimohazzab@uni-mainz.de; dandan.gao@uni-mainz.de
[b.] *Department of Materials Engineering and Metallurgy, Faculty of Engineering, Arak University, Arak 3815688349, Iran.*
Electronic Supplementary Information (ESI) available.
See DOI: 10.1039/x0xx00000x

including high surface area, high electrical conductivity and tunable reactivity.[35] Triggered by the pioneering studies on graphene and graphene exfoliation, a multitude of 2D layered nanomaterials have been developed, including transition metal dichalcogenides (TMDs), metal oxides, metal organic frameworks (MOFs), layered double hydroxides (LDHs), transition metal carbides/nitrides (MXenes), and hexagonal boron nitride (h-BN).[36, 37] The emergence of 2D nanomaterials with unique electrochemical and electronic properties has sparked research interest in biomass valorization coupled with H_2 production. In order to endow 2D nanomaterials with further improved catalytic performance, a wide range of design strategies have been developed including the heterojunction of two distinct materials, structure manipulation (e.g. doping and

defect/vacancies engineering), and rational integration of 2D nanomaterials on three-dimensional (3D) supports.[38, 39]

View Article Online
DOI: 10.1039/D4SE01034E

Herein, this review reports recent developments in the field of 2D nanomaterials for hybrid water electrolysis (**Figure 1**). Rational 2D nanomaterial design strategies are reviewed from host structure remodeling (heteroatom doping, defect/vacancy engineering and co-catalysts engineering) to structure assembly design (construction of heterostructure, surface engineering and 2D nanomaterials integrated into the 3D matrixes). Each design strategy is followed with a review of (photo-)electro-oxidation of HMF, glucose, and lignin coupled with H_2 production. Additionally, current challenges and emerging research directions have been pointed out.
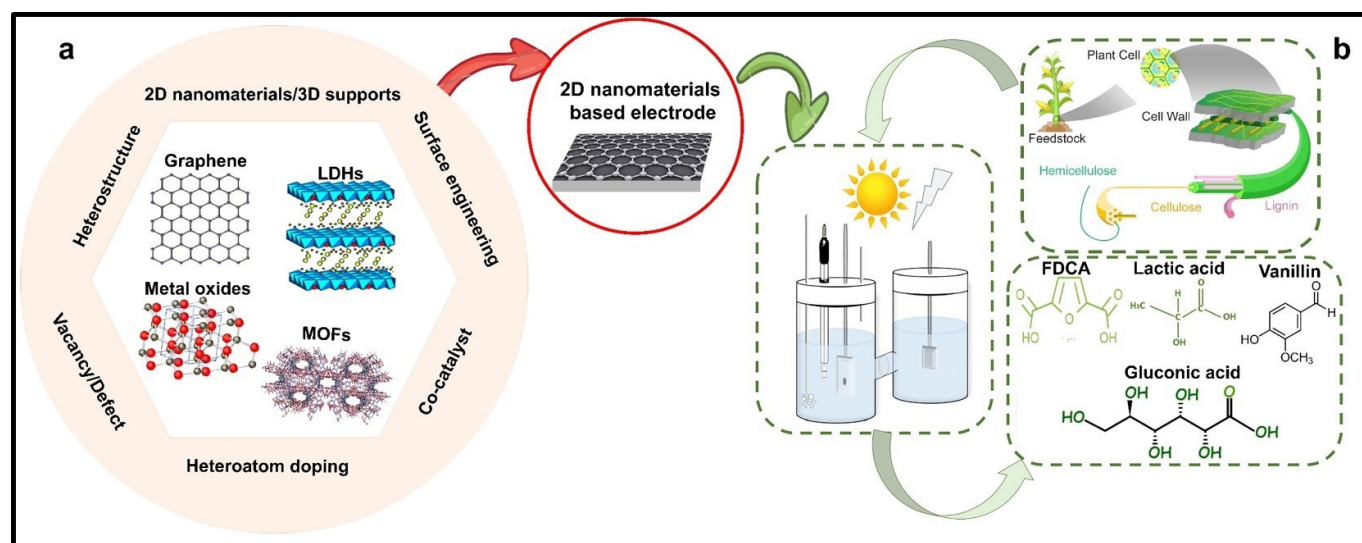
Fig. 1. Graphical illustration of the scope of this review: (a) 2D nanomaterial categories and design strategies and (b) employment of 2D nanomaterials in hybrid water (photo-)electrolysis. The 2D nanomaterial categories and lignocellulosic biomass cell wall have been adapted from Ref.[39] and Ref.,[40] with permission from MDPI and frontiers, copyright 2022, respectively.

2. 2D nanomaterials: design strategies and applications in hybrid water electrolysis

### 2.1. Host structure remodeling

2.1.1. Heteroatom doping

In general, doped nanostructures can be formed by replacing a specific atom in the support structure with another appropriate atom (known as a dopant atom).[41] Heteroatom doping modifies materials' properties by introducing dopants that alter electronegativity, valency, coordination, conductivity and band structure.[42, 43] Furthermore, doping can adjust the balance between the electronegativity and bond energy, creating potential active sites and therefore enhancing the material's reactivity.[44]

For PEC applications, in the case of semiconductors, doping is able to enhance light absorption optical range by multiple methods such as (1) introducing mid-gap states, (2) narrowing band gap and (3) forming impurity band.[45] Doping introduces mid-gap shallow or deep-level states which broaden the light absorption edge to longer wavelengths.[46] The mid-gap deep-level states contribute to extending light absorption, these states do not participate in visible-light photocatalytic activity and act as recombination centers mostly due to the lowest mobility of charge carriers.[47] On the contrary, the mid-gap shallow-level are capable of increasing charge carrier diffusion length and mobility.[48] In the case of noble metal doping, such as gold and silver, the semiconductor experiences the localized surface plasmon resonance (LSPR) effect. This LSPR effect results in enhanced light absorption in the near-infrared region which is beneficial for turning light into energy.[49]

For EC applications, in one instructive example, Wei *et al.*[50] designed Bi-doped Co_3O_4 nanosheet array on Ni foam (BiCoO-NA/NF) for 5-hydroxymethyl furfural oxidation reaction (HMFOR) coupled with HER. In the study, complete conversion of HMF to FDCA (Faradaic efficiency (FE): 97.7%, yield: 362.5 μmol h⁻¹) and promotion of H_2 production (yield: 7.33 μmol h⁻¹) can be simultaneously achieved at a low cell voltage of 1.3 V. The outstanding electrocatalytic performance is attributed to the heteroatom doping which provides fast mass/electron transfer channels and thus reduces the energy consumption. In a related study, Zhang *et al.*[51]

synthesized Cu-doped $Ni(OH)_2$ nanosheets ($(Ni_{1-x}Cu_x(OH)_2)_n$, in which Cu presented an island-like elemental distribution (**Figure 2a**). The optimum Cu doping led to $Ni_{0.9}Cu_{0.1}(OH)_2$, deriving higher performance toward HMFOR in comparison to OER (**Figure 2b**). Particularly, the $Ni_{0.9}Cu_{0.1}(OH)_2$ realized the HMFOR to FDCA with a 91.2% FE at 1.45 V vs RHE. The high selectivity for HMFOR is attributed to the formation of more active Ni^{3+} species and the coordination of unsaturated amorphous Cu species which are OER inert.
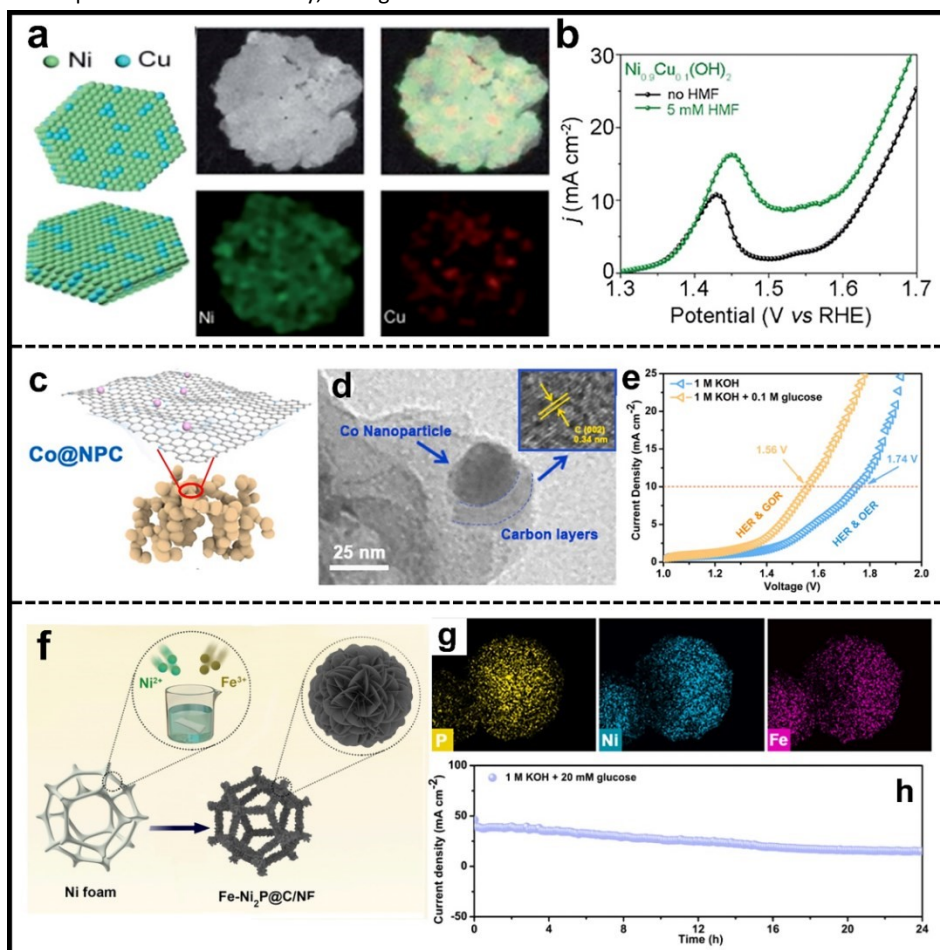
Fig. 2. Selected examples for **Heteroatom doping** subsection: (a) Schematic illustration of the $Ni_{1-x}Cu_x(OH)_2$ nanosheets and elemental distribution, (b) LSV curves comparison of $Ni_{0.9}Cu_{0.1}(OH)_2$ with and without HMF (These figures have been reproduced from Ref.[51] with permission from Royal Society of Chemistry, copyright 2021), (c) the schematic illustration and (d) TEM images of Co@NPC, (e) LSV curves of Co@NPC for GOR and OER coupled with HER (These figures have been reproduced from Ref.[52] with permission from Elsevier, copyright 2021), (f) the schematic representation and (g) elemental distribution of Fe-Ni_2P@C/NF electrode, and (h) The chronopotentiometry curve of Fe-Ni_2P@C/NF || Fe-Ni_2P@C/NF in 1 M KOH with 20 mM glucose (These figures have been reproduced from Ref.[53] with permission from Elsevier, copyright 2022)

In addition, Li *et al.*[52] investigated the glucose oxidation reaction (GOR) coupled with HER over cobalt nanoparticles supported on N-doped porous carbon (Co@NPC-T, T: calcination temperature, **Figures 2c** and **2d**). The activity of Co@NPC-800 were evaluated in a two-electrode cell, in which the presence of glucose resulted in

reduced cell voltage, for example, by 180 mV at the current density of 10 mA cm⁻² (**Figure 2e**). Products analysis indicated lactic acid (LA) and FA were the primary GOR products, with smaller amounts of GLA and GUA. According to DFT calculations, N doping improved glucose adsorption and optimized H_2O adsorption, thereby promoting GOR

and HER performance. Furthermore, Li *et al.*[53] synthesized bifunctional Fe-doped Ni_2P nanosheets hybridized with C on Ni foam (Fe-Ni_2P@C/NF) for the GOR and HER (**Figures 2f** and **2g**). Additionally, the chronoamperometry experiments conducted on the two-electrode electrolyzer with glucose addition showed that the current decreased to around half of its initial level after 24 h, indicating that sustaining glucose conversion during electrolysis (**Figure 2h**). The electrode showed sustained stability for 24 h and achieved a high current density of 100 mA cm^{-2} at a cell voltage of ca. 1.55 V. The electrolysis resulted in complete glucose conversion to LA and FA with a yield of 52.1% and 35.6%, respectively. A high FE of 98.2% for HER was observed in the hybrid water electrolysis system. DFT calculation indicated that Fe doping optimized the adsorption energy of H_2O molecules and the free energy of H_2 adsorption which facilitates the HER performance.

Moreover, heteroatom doping has also widely applied for the lignin oxidation reaction (LOR). For example, Cui *et al.*[54] reported the use of single atom Pt catalyst anchored on N-doped carbon nanotubes (Pt_1/N-CNTs) anode for selective electrocatalytic C–C bond cleavage in lignin, coupled with promoted H_2 production on a glassy carbon cathode. The Pt_1/N-CNTs exhibit unique electronic structures due to the increase in unsaturated coordination number, resulting in the raised active sites number. Remarkably, the high dispersion degree of the Pt single atom improved the atomic utilization, leading to the increased activity per unit catalyst. Altogether, the Pt_1/N-CNTs demonstrates outstanding selectivity in lignin electrochemical oxidative cleavage of C-C bonds for aromatic monomer formation. In a related study, Hao *et al.*[55] employed an electrochemical redox ion, $[Fe(CN)_6]^{3-}$, into PbO_2 matrix by electro-deposition method. The $[Fe(CN)_6]^{3-}$ doped PbO_2 electrode boosts a service lifetime of 287.25 hours, nearly triple that of standard PbO_2, and a 45% higher rate of alkali lignin degradation. This is attributed to a more compact surface and larger grain size, resulting in increased average cross-sectional area of pores. These structural improvements lead to greater stability and a higher electrochemical active surface area, enabling more efficient reactions. This pioneering work opens a new avenue for next-generation 2D electrocatalyst design for robust lignin electrolysis.
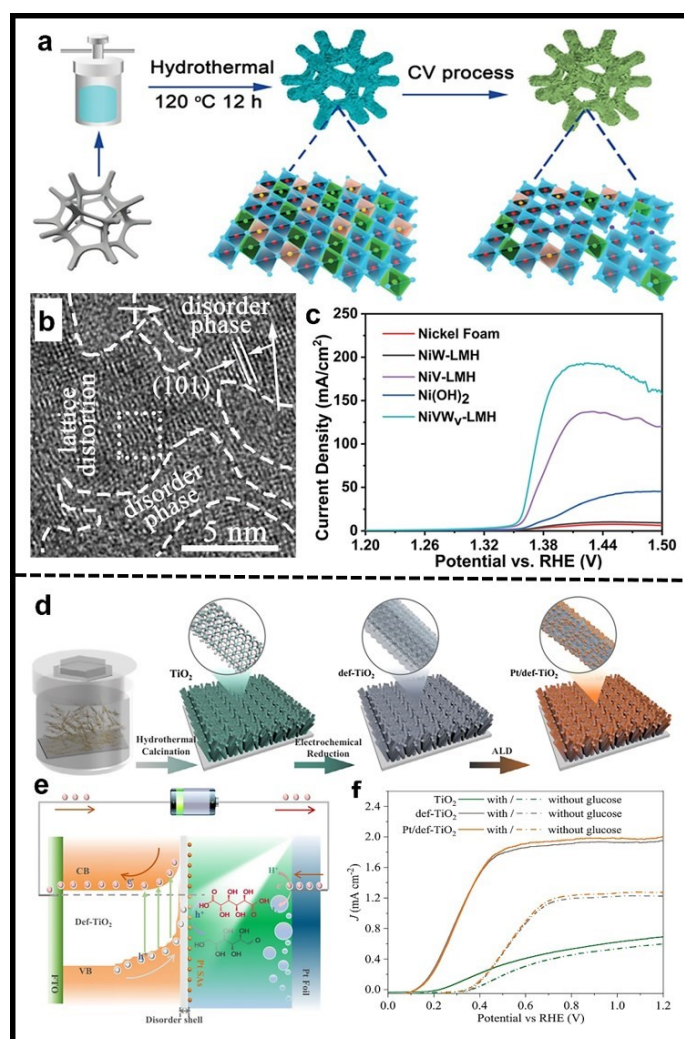
2.1.2. Defect/vacancy engineering

Defect engineering is known to enhance catalytic activity from structural destruction by modulating the electronic and surface properties of catalysts. And the defects obtained can be dimensionally classified into four categories (ESI, **Figure S3a**):[56] (i) point defects, resulted from introducing vacancy/doping and reconstruction of the structure, (ii) line defects, attributed to the dislocation of atoms in the host structure, (iii) planner defects, generated from lattice deviation along the in-plane direction, (iv) volume defects, led by spatial lattice disorder in the whole body phase. Notably, these categories influence 2D nanomaterial properties in different ways. For example, point defects alter the local electronic and reactive properties, while line defects affect the

structural and mechanical properties by disrupting the symmetry and continuity. Furthermore, planner and volume defects can drastically alter the properties of 2D materials via inducing phase transitions, changing the dimensionality, and creating hybrid structures. In particular, point defects have been widely applied to modify 2D nanomaterials owing to their ability to locally tune the physical and chemical properties of catalysts.[57, 58]

In PEC pathway, defects can be located in the bulk phase or on the surface of semiconductors, resulting in volume and planner defects, respectively. They affect the photo-electrocatalytic process in different ways (ESI, **Figure S3b**). For instance, planar defects within the photo-electrocatalyst can act as traps for holes, enhancing charge separation by preventing immediate recombination with electrons. These trapped holes can then react with electron donors on the catalyst's surface, leading to the desired chemical reactions. Conversely, volume defects may trap both electrons and holes, potentially leading to recombination, which is counterproductive for photo-electrocatalytic activity.[59] Therefore, the generated charge carriers could be trapped by volume or planner defects, resulting in recombination or reactions participation, respectively.[60] It should be noted that excessive vacancies can reduce reaction efficiency resulted from unfavourable charge carrier recombination. Therefore, moderate vacancies in 2D nanomaterials design is desired to rationalize visible light absorption, electron-hole pair generation, and hydrogen adsorption.[61]

For applications, Zhang *et al.*[62] developed a series of ternary NiVW layered metal hydroxides electrocatalysts with abundant lattice vacancies (NiVW$_v$-LMH) for the HMFOR (**Figure 3a**). Remarkably, the NiVW$_v$-LMH nanosheets obtained lattice-disordered phases and vacancies after 50 cyclic voltammetry (CV) cycles (**Figure 3b**), which demonstrated a high current density of 193 mA cm^{-2} for HMOR to FDCA with a 100% conversion rate at 1.43 V vs. RHE (**Figure 3c**). The high performance is attributed to the dissolution of V and W which changes the local coordination of Ni cations and increases the amount of unsaturated active sites. In another study, Zhu *et al.*[63] synthesized a $CuMn_2O_4$ spinel electrocatalyst for HMFOR using hydrothermal deposition approach followed by ammonia etching to create oxygen vacancies. The ammonia-etched $CuMn_2O_4$ achieved a current density of 20 mA cm^{-2} at 1.31 V vs. RHE. A 100% conversion rate and 96% selectivity to FDCA were observed. Moreover, Tian *et al.*[64] studied PEC hybrid water electrolysis using single-atom Pt on defective TiO_2 nanorod arrays (Pt/def-TiO_2 RNAs) for GOR coupled with HER (**Figures 3d** and **3e**). The prepared Pt/def-TiO_2 RNAs reached a high photocurrent density of 1.91 mA cm^{-2} at 0.6 V vs. RHE (**Figure 3f**). After 5.5 h of GOR, 98.8% of glucose was converted into GLU and GLA with a yield of 84.3% and 9.2%, respectively. And a high FE of 99% was observed for the HER. The TiO_2 defective structure led by oxygen vacancy promotes charge dynamic for PEC GOR by facilitating charge movement. The def-TiO_2 possesses large electron conduction band and large surface band bending which are favorable properties for charge carrier movement and extraction.

Fig. 3. Selected examples for **Defect/vacancy engineering** subsection: (a) Synthetic route of NiVW$_v$-LMH crumpled nanosheets, (b) HR-TEM image of NiVW$_v$-LMH, (c) LSV curves of NiVW$_v$-LMH after 50th CV cycle with 90% *iR* correction (These figures have been reproduced from Ref.[62] with permission from Wiley, copyright 2023), (d) fabricating process for the TiO$_2$, def-TiO$_2$, and Pt/def-TiO$_2$ NRAs, (e) energy band diagram of Pt/def-TiO$_2$ NRAs photoanode and charge carriers' movement during GOR and HER process, and (f) LSV profiles of prepared photoanodes for GOR under AM 1.5 G, 100 mW cm^{-2} illumination (These figures have been reproduced from Ref. [64] with permission from Nature, copyright 2023).

2.1.3. Co-catalysts engineering

Coating the catalyst surface with a co-catalyst is a prominent tool to boost the catalytic activity. The co-catalysts participate in electrochemical oxidation/reduction by providing active sites for the reactions between charge carriers and intermediate ions (e.g. H$^+$ or OH$^-$). In order to enhance overall water (photo-)electrolysis performance, Rh, Pt, Ru, and Ir metals and oxides of Fe, Co, Ir, Ru, and Ni have been utilized as co-catalysts for HER and OER, respectively.[65]

In PEC systems, the integration of a co-catalyst is crucial for promoting charge separation and enhancing transport at the semiconductor-co-catalyst interface.[66] The addition of the co-catalyst leads to the formation of a space-charge region, which in turn establishes a semiconductor/co-catalyst junction, commonly

referred to as a Schottky barrier.[67] At this junction, the alignment of Fermi energy levels initiates electron migration. The direction of electron movement and the resultant band bending are influenced by the relative Fermi levels of the materials in contact. Typically, for an n-type semiconductor combined with a metal co-catalyst possessing a higher work function, there is a flow of electrons from the semiconductor to the metal. This electron flow induces upward band bending, propelling electrons toward the space-charge region, while holes tend to accumulate on the photo-electrocatalyst's surface.[68] The formation of the Schottky barrier is instrumental in mitigating electron-hole recombination, thereby significantly improving PEC efficiency. It is essential to recognize that the precise direction of electron flow and band bending is contingent upon the specific energy levels of the materials involved (ESI, **Figure S3c**). Despite the high activity of noble metals, earth-abundant 2D noble-metal-free co-catalysts have emerged in recent years attributed to

the low cost, tunable composition, superior structural stability and tailorable reactivity.[69]
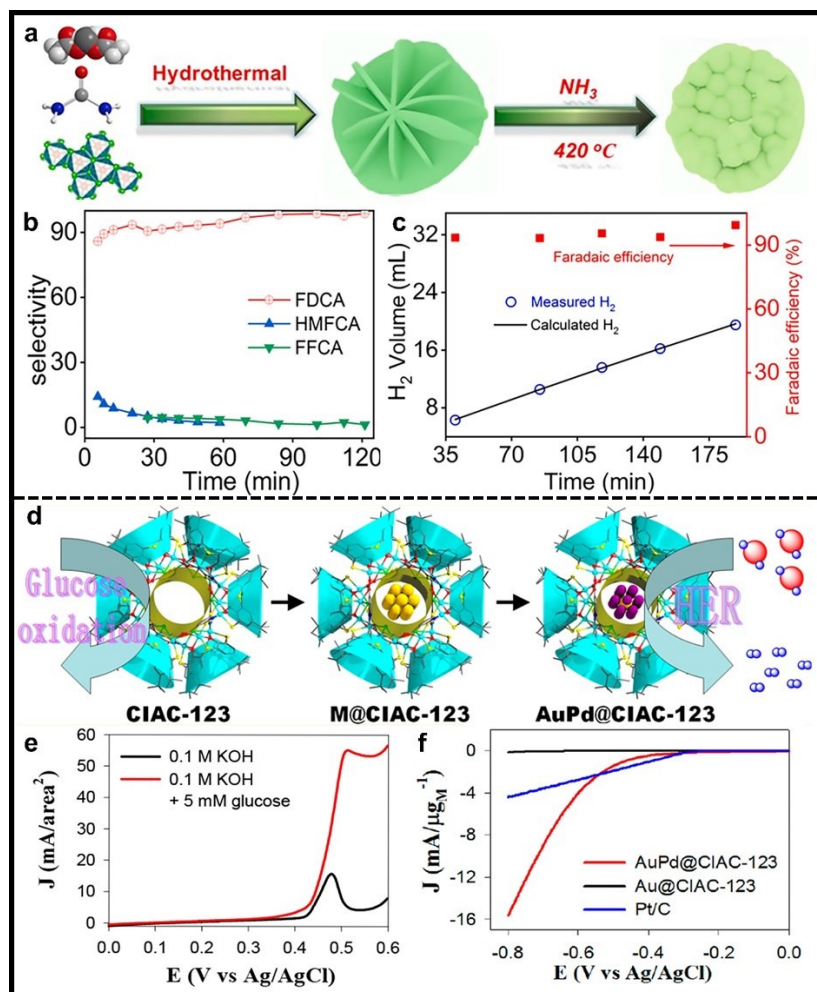
Fig. 4. Selected examples for **Co-catalysts engineering** subsection: (a) Synthetic route of the Ni_3N-V_2O_3 electrode, (b) HMFOR selectivity for FDCA, HMFCA and FFCA, (c) hydrogen production and faradaic efficiency for HER as a function of electric charge (left axis) and electric current (right axis) (These figures have been reproduced from Ref.[70] with permission from Elsevier, copyright 2021), (d) Schematic illustration of the wheel structure of CIAC-123, M@CIAC-123, and AuPd@CIAC-123, M: tiny metal nanoclusters such as Au, Pd, Ir, Ru, Rh, Pt, and AuPd, (e) LSV curves of CIAC-123 in 0.1 M KOH with or without 5 mM glucose, and (f) LSV curves of the AuPd@CIAC-123, Au@CIAC-123, and the commercial Pt/C in 0.5 M H_2SO_4 for HER (These figures have been reproduced from Ref.[71] with permission from American Chemical Society, copyright 2018)

Liang *et al.*[70] employed Ni_3N-V_2O_3 as a potent co-catalyst for HMFOR-assisted HER (**Figure 4a**), which demonstrated high FDCA selectivity (98.7%) and yield (96.1%) as well as advanced HER performance (**Figures 4b** and **4c**). The co-catalyst engineering altered the electronic structure and reduced the band gap energy, leading to low cell voltage (1.40 V at 10 mA cm^{-2}) and 100% FE of HER in hybrid water electrolysis. For GOR application, Ru and Ir nanoclusters and their oxides have been extensively employed due to their structural and chemical stability, as well as their superior electrocatalytic activity. For example, Chen's group[71] developed a novel calixarene-based {Ni_{18}} coordination wheel entity (CIAC-123) as an efficient

bifunctional electrocatalyst for GOR and HER (**Figure 4d**). Promisingly, the open-wheel structure can serve as a template for encapsulation and fabrication of tiny metal nanoclusters such as Au, Pd, Ir, Ru, Rh, Pt, and AuPd. As observed, the CIAC-123 performed as an efficient catalyst for GOR while bimetallic AuPd@CIAC-123 exhibited significantly improved HER performance (**Figures 4e** and **4f**). Considering the size of pore diameter (0.9 nm) in AuPd@CIAC-123 and glucose molecule diameter (~1 nm), it could be concluded that the presence of AuPd limits the accessibility of the inner cavity to glucose molecules, while hydrogen ions can pass through the cavity for the absorbance. Therefore, based on the size of molecules,

the Ni sites are responsible for GOR while HER activity can be attributed to Pd sites with synergistic effects of Au and Ni.

Co-catalyst engineering has also been employed to explore advanced catalysts for efficient LOR. In this regard, Rauber et al.[72] coated a third metal (Mn, Pd, V, or Ti) in mixed Ru-Ir oxides ($Ru_{0.2}Mn_{0.2}Ir_{0.6}O_x$, $Ru_{0.2}Pd_{0.2}Ir_{0.6}O_x$, $Ru_{0.2}V_{0.2}Ir_{0.6}O_x$ and $Ru_{0.2}Ti_{0.2}Ir_{0.6}O_x$). Compared to the initial binary metal oxide ($Ru_{0.4}Ir_{0.6}O_x$), the co-existence of the third metal, particularly for Mn metal, can significantly improve the yield of monomers from LOR. In one related investigation, the Gao group modified the NiFeO arrays fabricated on Ni foam with Ir single atoms (Ir-NiFeO@NF) for efficient 1-phenylethanol (a simple lignin model) valorization and H_2 production.[73] It showed that deployment of the bifunctional Ir-NiFeO@NF in a two-electrode cell can reach the current density of 10 mA cm^{-2} at 1.33 V. Additionally, the H_2 production rate of ca. 0.45 mmol h^{-1} cm^{-2} was observed with a FE close to 100% at the applied cell voltage of 1.5 V. Anodic products analysis revealed that lignin motifs were transformed into benzoic acids.

2.2. Structure assembly design

2.2.1 Construction of heterostructure

Heterostructures are structures in which different components are linked together by heterogeneous interfaces or heterojunctions (e.g., semiconductor-carbon nanomaterials).[74, 75] The design of heterostructures can alter the number of active sites, lattice strain, and electronic structure due to interfacial changes.[76, 77] In particular, modulated electronic structure can enhance the adsorption/desorption of catalyst reaction intermediates, thereby increasing the electrocatalytic activity.[78] Furthermore, it is well-documented that a larger contact area can accelerate the charge carriers' movement and create sufficient transporting channels at the interfaces of heterostructures.[79] Remarkably, heterostructures with various dimensions exhibit diverse interfacial contacts such as point contact (0D-2D), line contact (1D-2D) and face contact (2D-2D).[79] Among them, the face contact in 2D-2D heterostructure is an ideal condition to re-localize electrons and improve redox ability.[80] Details about the contact interfaces of synergistic nanostructures as well as synthetic methodologies have been previously reviewed.[81, 82]

For PEC applications, primary objectives of heterostructure design are to prevent charge recombination while promote charge movement and separate electron-hole pairs using diverse charge transfer mechanisms. The efficiency of PEC processes is enhanced through improved charge-carrier separation, enriched active sites, and optimized reaction conditions facilitated by heterostructure design.[83] Based on the position of the conduction band (CB) and valence band (VB), these mechanisms are often categorized into five groups: p-n junction, type I, type II, Z-scheme and S-scheme.[7, 8, 84, 85] Notably, the charge transfer mechanism differs when incorporating carbon-based materials into the photo-electrocatalysts heterostructure.[68] For instance, when a graphene-based heterostructure is irradiated with light, the semiconductor generates

charge carriers, which then transfer electrons from the CB of the semiconductor to the graphene sheets, resulting in a reduction reaction. Meanwhile, the remaining holes in the VB of the semiconductor participate in oxidation reactions. A schematic of charge transfer mechanism of graphene-semiconductor is available in ESI, **Figure S3d**.

In (photo-)electrocatalysis, heterostructure design renders (photo-)electrocatalyst high surface area and strong interfacial contact. In this context, the charge carriers generated during the reaction can be quickly and efficiently transported away from the active sites, thus enhancing the overall reaction rate. As a prime example, Sun et al.[86] investigated the coupling of HMFOR and HER using a heterostructured nanorod array electrocatalyst deposited on Ni foam (Ni/Ni$_{0.2}$Mo$_{0.8}$N/NF), which demonstrated excellent activity toward both HMFOR and HER. Remarkably, the hybrid water electrolysis system employing the bifunctional Ni/Ni$_{0.2}$Mo$_{0.8}$N/NF electrode only required 1.51 V for a current density of 50 mA cm^{-2}. And products analysis showed 98.5% yield for FDCA. This superior performance was attributed to electronic structure modulation and robust contact between Ni foam support and Ni$_{0.2}$Mo$_{0.8}$N. In another example by Zhong et al.[87], Ni$_x$Se$_y$ nanowire arrays shelled with NiFe LDH nanosheets (named Ni$_x$Se$_y$–NiFe LDH@NF) was applied for HMFOR couple with HER on Pt sheet. In the reported heterostructured Ni$_x$Se$_y$–NiFe LDH@NF, Ni$_x$Se$_y$ nanowire core facilitated fast charge transfer while NiFe LDH nanosheets provided a large surface area with abundant active sites (**Figures 5a** and **5b**). To this end, the HMFOR activity of the Ni$_x$Se$_y$–NiFe LDH@NF was significantly promoted, leading to substantially reduced overpotentials as compared to presented reference materials (**Figure 5c**). In addition, high yield of 99.3% and FE of 98.9% were observed for HMFOR to FDCA at 1.42 V vs. RHE. Moreover, Deng et al.[88] modified copper sulfide core nanowire grown on Cu foam with NiCo-layered double hydroxide outer-shell nanoarrays (Cu$_x$S@Ni$_{0.75}$Co$_{0.25}$O$_x$H$_y$/CF) for simultaneous HMFOR and HER (**Figures 5d - 5f**). The hybrid electrolysis system only required a cell voltage of 1.34 V to reach 10 mA cm^{-2}, which is lower than HMF-absent system by 0.27 V (**Figure 5g**). Notably, the Cu$_x$S@Ni$_{0.75}$Co$_{0.25}$O$_x$H$_y$/CF achieved complete HMF conversion to FDCA with 100% FE at 1.3 V vs. RHE and a unity FE for HER. The open core-shell structure of nanoarrays provided a large number of active sites, which facilitated mass transfer. Furthermore, the incorporation of Co adjusted the electronic structure of Ni to a higher content of Ni^{3+}, which accelerated the adsorption of reactants and intermediates. The synergetic effect between designed specific nanostructure and modulated electronic structure is beneficial for the improved performance.

In addition, Sun et al.[89] designed hetero- nanoparticles (Fe$_3$O$_4$/Au) distributed on basal plane of CoFe-LDH, leading to Fe$_3$O$_4$/Au/CoFe-LDH with heterostructures for efficient GOR coupled with HER (**Figures 5h** and **5i**). This study highlighted that the presence of Fe$_3$O$_4$ and CoFe-LDH in the sandwich structure boosted the electrochemical activity of Au nanoparticles in GOR by regulating its electronic

ARTICLE

structure and providing a large surface area. In this context, the Fe₃O₄/Au/CoFe-LDH heterostructures displayed significantly reduced cell voltages for GOR/HER compared to OER/HER (**Figure 5j**). In particular, the current density of 50 mA cm⁻² led to full conversion of glucose to gluconate and HER with FE of ca. 99.6%. Moreover, Bateni *et al.*[90] integrated PbO₂ nanoparticles into high surface area multi-walled carbon nanotubes (PbO₂/MWNTs) via impregnation method for electrochemical LOR (**Figure 5k**), which showed boosted rates in terms of both LOR and HER (on Pt black cathode) in a lignin electrolysis cell. Additionally, the comparison of current densities at the same potential shows that increasing catalyst loading from 8 to

10 mg cm⁻² significantly enhanced the performance due to the change in the number of accessible active sites (**Figure 5l**), while further increase in catalyst loading (12 mg cm⁻²) cannot yield higher performance. In another work, the electroactivity of a NiCo electrocatalyst was improved towards lignin-assisted water electrolysis by fabricating a NiCo/TiO₂ heterostructure electrocatalyst as an anode while Pt nanoparticles loaded on a carbon cloth as an cathode.[91] The results reported that at the cell voltage of 1.6 V, the current density and the FE of H₂ evolution reached 10 mA cm⁻² and 99%, respectively. Furthermore, the gas product analysis revealed 100% purity of H₂.
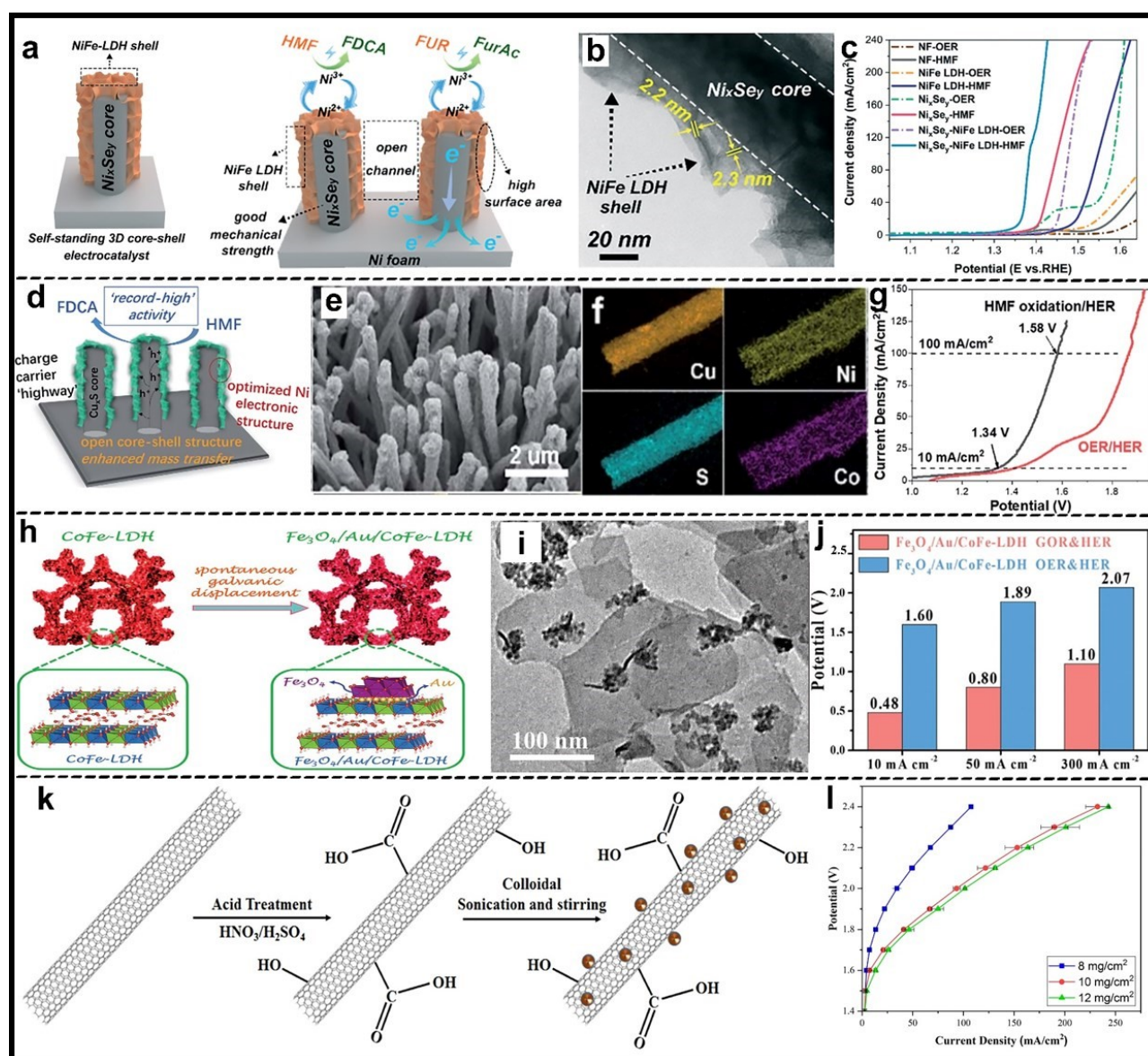
Fig. 5. Selected examples for **Construction of heterostructure** subsection: (a) The schematic structure and the mechanism proposed for the electrooxidation of HMF and furfural (FUR) on NiₓSeᵧ–NiFe LDH@NF electrode, (b) TEM images of NiₓSeᵧ–NiFe LDH core–shell structure (c) LSV curves of NF, NiFe LDH@NF, NiₓSeᵧ@NF and NiₓSeᵧ-NiFe LDH@NF (These figures have been reproduced from Ref.[87] with permission from Royal Society of Chemistry, copyright 2022), (d) schematic illustration, (e) SEM image and (f) elemental mapping of CuₓS@Ni₀.₇₅Co₀.₂₅OₓHᵧ/CF, (g) LSV curves for OER/HER and HMFOR/HER over bifunctional CuₓS@Ni₀.₇₅Co₀.₂₅OₓHᵧ/CF electrode (These figures have been reproduced from

Ref.[88] with permission from Royal Society of Chemistry, copyright 2020), (h) Synthetic route and (i) TEM image of CoFe-LDH and Fe$_3$O$_4$/Au/CoFe-LDH, (j) cell potential of GOR/HER and OER/HER at different current densities with iR-compensation (These figures have been reproduced from Ref.[89] with permission from Wiley, copyright 2021), (k) synthetic approach for PbO$_2$/MWNTs for LOR, and (l) LSV curve from different PbO$_2$/MWNTs catalyst loadings samples (These figures have been reproduced from Ref.[90] with permission from IOP Publishing, copyright 2019)

2.2.2 Surface engineering

As aforementioned in heterostructure design strategy, highly efficient catalyst interfaces render promoted electrocatalytic performance. In this context, surface morphology and wettability are considered as crucial parameters. Compared to smooth surfaces, micro- and nanostructured catalyst surfaces are able to expose more active sites, shorten the transport distance of charge carriers, and increase the absorption of light to generate and separate charge carriers by reflection or scattering.[92, 93] For example, compared to

BiVO$_4$ flat films, adjusting the distance between BiVO$_4$ nanosphere to match the incident light wavelength traps and scatters light, can substantially enhance the light-driven capability and interface accessibility (ESI, **Figure S3e**).[94] Furthermore, high wettability is desirable by rational surface engineering, which enables efficient gas bubbles release, high utilization of surface active sites and therefore strong interaction between catalyst interface and electrolyte. For this purpose, superaerophobic and superhydrophilic surface coatings are always built by researchers.[95]
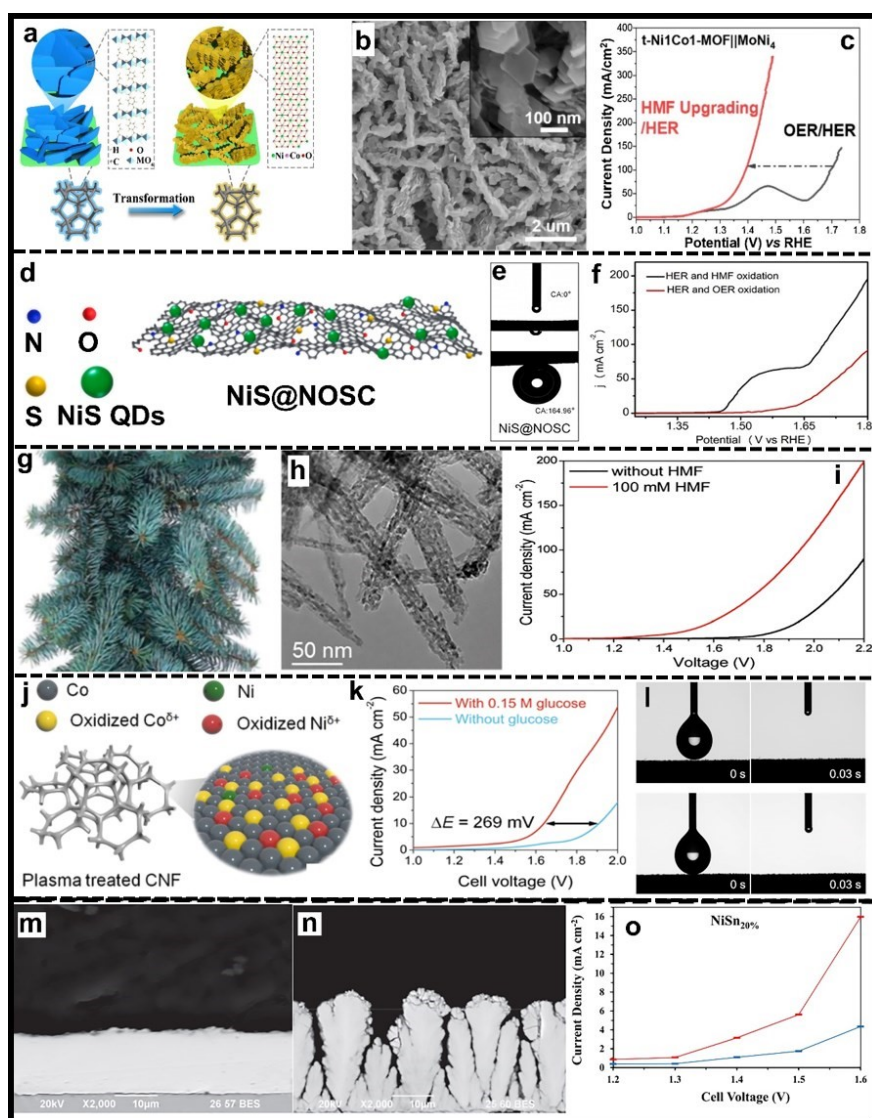
Fig. 6. Selected examples for **Surface engineering** subsection: (a) The illustration of nanoplatelet-on-nanoarray t-NiCo-MOF electrocatalyst deposited on NF, (b) SEM images of transformed Ni1Co1-MOF (t-Ni1Co1-MOF) , and (c) LSV of t-Ni$_1$Co$_1$-MOF(anode)||MoNi$_4$(cathode) system for OER/HER and HMFOR/HER (These figures have been reproduced from Ref.[96] with permission from Elsevier, copyright 2020), (d) Illustration of the synthesis procedure of NiS@NOSC, (e) static-water-droplet contact angles for under-water air-bubble contact angles on the surface of NiS@NOSC, (f) LSV curves of NiS@NOSC||NiS@NOSC for OER/HER and HMFOR/HER (These figures have been reproduced

from Ref.[97] with permission from Elsevier, copyright 2022), (g) Photo of a pine needle, (h) TEM image of morphological features of the exfoliated CoNW, (i) LSV curves of two-electrode system (CoNW/NFs ||CoNW/NFs) with and without HMF (These figures have been reproduced from Ref.[98] with permission from Royal Society of Chemistry, copyright 2019), (j) schematic illustration of the modification of CNF via O_2 plasma treatment, (k) LSV of CNF-60||CNF-60 system for GOR coupled with HER, (l) changes in the wetting behavior of the surface: (top row) pristine CNF and (down row) CNF after 60 minutes (CNF-60) of plasma exposure (These figures have been reproduced from Ref.[99] with permission from Royal Society of Chemistry, copyright 2023), cross-section image of Ni (m) and NiSn_{20%} (n), (o) current density as a function of cell voltages for NiSn_{20%} in 1 M NaOH solution (absent lignin: blue plot and presence lignin: red plot) (These figures have been reproduced from Ref.[100] with permission from IOP publishing, copyright 2020)

For the applications of surface engineering design strategy, Deng *et al.*[96] reported a hexagonal nanoplatelet-on-nanoarray NiCo hydroxide-based electrocatalysts (t-NiCo-MOF) for HMFOR coupled with HER on $MoNi_4$ cathode (**Figures 6a** and **6b**). To achieve a current density of 100 mA cm^{-2}, the t-Ni$_1$Co$_1$-MOF||MoNi$_4$ hybrid electrolysis system requires a low cell voltage of 1.392 V, while the HMF-free system requires 1.7 V (**Figure 6c**). The product quantification highlighted complete conversion of HMF to FDCA with a high FE of 98%. The high activity and selectivity observed can be attributed to the reasonable morphology design, providing increased interfacial contact and facilitating mass transfer. In a related study, the Wang group[97] developed a bifunctional superhydrophilic/superaerophobic surface by depositing NiS quantum dots (QDs) into wrinkled N,O,S-tri-doped carbon porous nanosheets (NiS@NOSC) for simultaneous HMFOR and HER (**Figure 6d**). Static-water-droplet contact angles and underwater air-bubble contact angles (**Figure 6e**) revealed that the superhydrophilic and superaerophobic properties of the NiS@NOSC surface, accelerating electrolyte penetration and bubble release, respectively. As compared to OER/HER system, the HMFOR/HER system exhibited considerably reduced cell voltage, and only 1.51 V was required for reaching 50 mA cm^{-2} current density (**Figure 6f**). Remarkably, 100% conversion of HMF to FDCA was observed with a FE of ca. 99.6 % and a 100% FE for HER. In another example, Zhou *et al.*[98] employed pine needle-like Co_3O_4 nanowires on Ni foam (CoNW/NF, **Figure 6g**) as an efficient bifunctional electrocatalyst for HMFOR and HER. Benefiting from the porous nanorod-like leaves surface morphology (**Figure 6h**), abundant active sites can be exposed. This led to reduced cell voltage for the HMF-present system (**Figure 6i**). Specifically, after 5.73 h of HMFOR, complete conversion into FDCA with a yield of 96.8% and a FE of 96.6% were observed, together with a 100% FE for HER. The outstanding performance is attributed to the open nanowire structures that facilitated mass transfer, while the interconnected structures enhanced charge transfer process.

Additionally, the Augustynski group[101] proposed a nanostructured WO_3 photoanode for GOR coupled with HER, resulting in a variety of valuable products such as GLA, GUA, erythrose and arabinose. In this study, simultaneous GOR and HER at 1.23 V vs. RHE demonstrated a high photocurrent density of ca 6.5 mA cm^{-2} under stimulating AM 1.5 G. In another example, Wang *et al.*[99] employed ultrafast oxygen plasma to modify commercial Co-Ni foam (CNF) to give CNF-60 a superhydrophilic surface (**Figure 6j**) for GOR and HER. Compared to the pristine CNF, CNF-60 yielded higher current density at applied potentials higher than 1.45 V, suggesting more favorable mass

transferring of glucose. In the two-electrode (CNF-60||CNF-60) cell, reduced cell voltages can be observed in the presence of glucose, for example, by 269 mV at the current density of 10 mA cm^{-2} (**Figure 6k**). Moreover, water contact angle evaluation of the modified surface and pristine condition (**Figure 6l**) suggested that both materials possess superhydrophilic features. This indicates that the improved electrochemical performance is attributed to elemental changing resulted from the plasma treatment. Furthermore, Ghahremani *et al.*[100] reported LOR coupled with HER by co-electrodepositing Ni and Sn on a Ti substrate, leading to NiSn_{20%} alloy electrode showing cauliflower-like morphology with increased porosities and channels (**Figures 6m** and **6n**). Compared to the lignin-free condition, the obtained NiSn_{20%} demonstrated higher performance in the lignin-present system (**Figure 6o**). Additionally, it delivered a high H_2 production rate of 72 ml h^{-1} at a cell voltage of 1.6 V, while a remarkable targeting vanillin production rate of 300 g/kg lignin min^{-1} was observed at a cell voltage of 1.4 V.

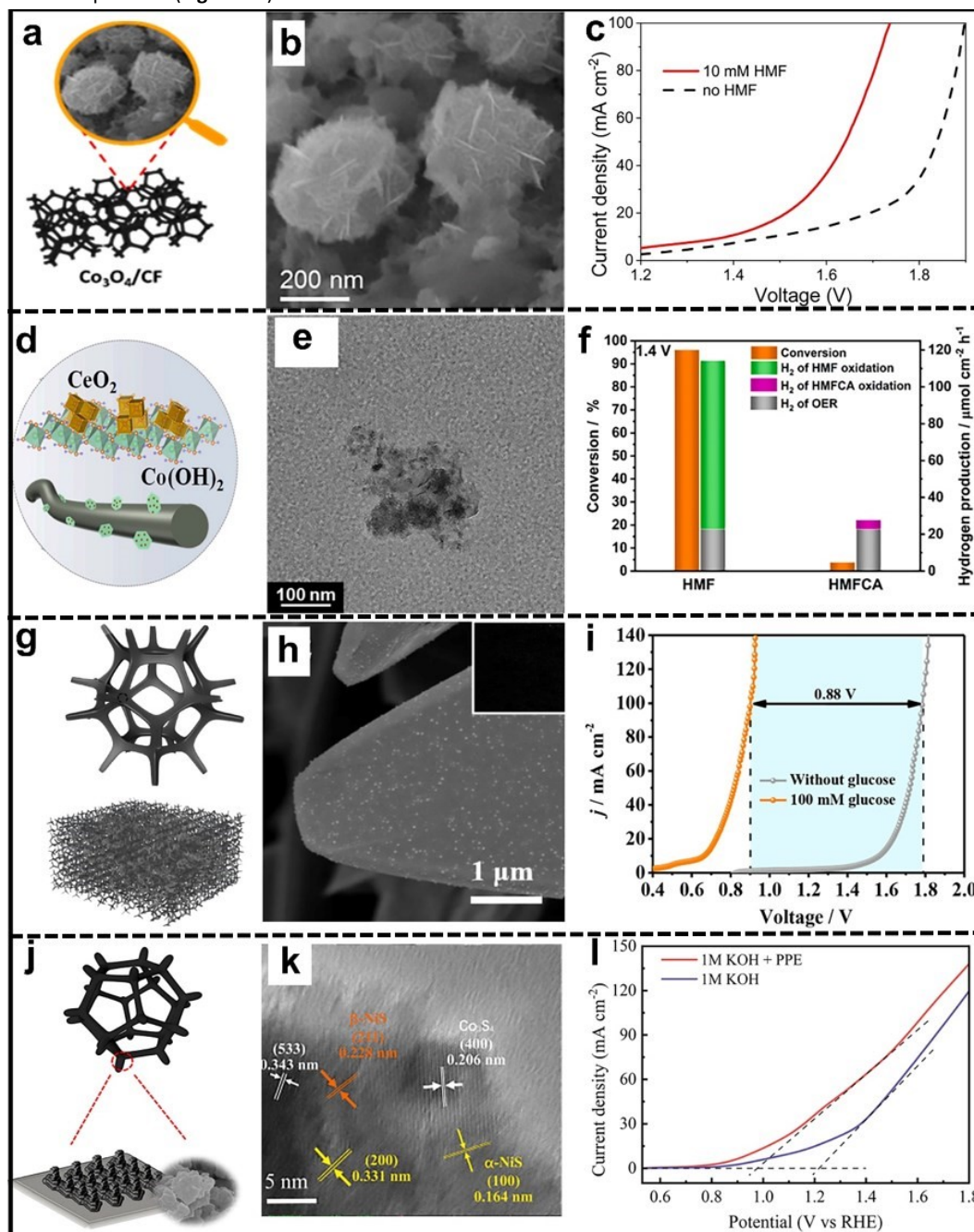### 2.2.3. 2D nanomaterials integrated into 3D matrixes

The recent development in electrode design has led to the integration of 2D nanomaterials with 3D porous substrates. This can significantly enhance the interfacial contact between the nanomaterials and substrate, thus improving electrical conductivity of resulting electrodes. Furthermore, the diffusion lengths for ions and electrons are effectively reduced, facilitating more efficient and direct pathways for charge transport and storage.[102-104] In this context, a variety of aligning orientations can be achieved including horizontal, vertical, heterogeneous and arbitrary structures.[35] In particular, metal foams featuring adjustable surface area and tunable surface morphology, have been widely applied to integrate 2D nanomaterials for energy conversion and storage systems.[105-110]

For example, Chen and coworkers[111] proposed electrochemically tuning the nonporous CoS_x deposited on Co foam to Co_3O_4 (Co_3O_4/CF, **Figure 7a**) for HMFOR and HER. The obtained Co_3O_4/CF exhibits a hierarchical structure consisting of microspheres and nanosheets distributed on the surface (**Figure 7b**). The cell voltage was significantly reduced when HMF was present in the hybrid electrolysis system (**Figure 7c**). Attributed to defective structures and abundant electroactive sites distributed on the 3D Co foam support, the bifunctional Co_3O_4/CF achieved complete conversion of HMF to FDCA with a high yield (93.2%), as well as high FEs for both HMFOR and HER (92.9% and 99.8%, respectively). Moreover, the Zhao group[112] synthesized a sheet-like cobalt hydroxide-cerium dioxide composite catalyst on carbon fiber paper (Co(OH)$_2$-CeO$_2$) for HMFOR

Journal Name

ARTICLE

coupled with HER (**Figures 7d** and **7e**). Through two-electron oxidation, HMF was converted to 2-furancarboxylic acid (HMFCA) with a selectivity of 89.4% and a yield of 85.8%. Promising hybrid water electrolysis was carried out at 1.4 V with optimized HMF conversion rate (96%) and boosted H_2 production rate (114.39 μmol cm^{-2} h^{-1}, **Figure 7f**). In addition, Xin *et al.*[113] anchored bifunctional size-controllable Co/Ni-co-doped carbon on Cu foam (CF@CoNC-xT, x represents the crystallization times) for GOR and HER (**Figure 7g**). The obtained CF@CoNC-2T electrode shows a rough surface distributed with Co nanoparticles (**Figure 7h**). The two-electrode cell

showed a cell voltage of only 0.9 V, which is 0.88 V lower than glucose-free system (**Figure 7i**). Additionally, a FE of 100% for HER and value-added product (GNA as well as GRA) were obtained. In another study by Liu and colleagues,[114] NiFeO$_x$ and NiFeN$_x$ were deposited on 3D nickel foam for GOR and HER, respectively. The optimized electrodes were able to deliver a current density of 200 mA cm^{-2} at a low cell voltage of 1.48 V. Meanwhile, the efficient conversion of glucose to GRA was observed with a high FE of 87% and yield of 83%.

Fig. 7. Selected examples for **2D nanomaterials integrated into 3D matrixes** subsection: (a) Illustration and (b) SEM image of the fabricated Co$_3$O$_4$/CF, (c) LSV curves of Co$_3$O$_4$/CF||Co$_3$O$_4$/CF system in the presence and absence of 10 mM HMF (These figures have been reproduced from Ref.[111] with permission from Elsevier, copyright 2022, (d) a schematic illustration and (e) TEM images of Co(OH)$_2$-CeO$_2$ electrode, (f) The conversion of HMF and HMFCA and corresponding H_2 production under a potential of 1.4 V using Co(OH)$_2$-CeO$_2$ electrode (These figures

have been reproduced from Ref.[112] with permission from Elsevier, copyright 2023), (g) a schematic illustration and (h) SEM image (inset: optical photograph of sample) of CF@CoNC-2T, (i) LSV curves of two-electrode cell consisting of CF@CoNC-2T||CF@CoNC-2T with and without glucose (These figures have been reproduced from Ref.[113] with permission from Royal society of chemistry, copyright 2022), (j) a schematic structure and (k) TEM image of NF@Co₃S₄/(α,β)-NiS, and (l) LSV curves of NF@Co₃S₄/(α,β)-NiS in 1.0 M KOH with and without 1.0 mM PPE (These figures have been reproduced from Ref.[115] with permission from Elsevier, copyright 2022)

Recently, Ni-based porous electrodes have been extensively developed for the LOR, owing to their low cost, high catalytic activity, and robust anti-corrosion stability.[116] Notably, under oxidative operation, Ni electrodes always form a catalytically active surface NiOOH layer, leading to enhanced lignin conversion performance.[117] In this regard, the Waldvogel group has reported series of studies on the anodic depolymerization of lignin on 2D planar or 3D porous Ni-based electrodes.[118-121] It is reported that the repeated use of Ni foam electrodes for LOR significantly increased vanillin production, indicating an activation phenomenon from the *in situ* deposition of a modified layer on the electrode surface (ESI, **Figure S4**).[117] In addition, Wang *et al.*[115] fabricated self-supported Co and Ni bimetallic sulfides on Ni foam (NF@Co₃S₄/(α,β)-NiS, **Figure 7j**) for the oxidation of 2-phenoxy-1-phenylethanol (PPE), a typical β-O-4 lignin model compound coupled with Pt catalyzed HER. The structural analysis demonstrates that Co₃S₄ is stacked in a lamellar structure with pore channels which facilitate mass transfer rate (**Figure 7k**). At the same current density (i.e., 10 mA cm⁻²), the potential of PPE oxidation (0.954 V vs. RHE) was considerably lower than that of PPE-free system (i.e., 1.107 V vs. RHE, **Figure 7l**). Meanwhile, a large amount of H₂ bubbles produced at the cathode were observed.

3. Current challenges and emerging strategies

This review reports on recently developed design strategies for 2D nanomaterials based (photo-)electrocatalysts for biomass valorization coupled with H₂ evolution, of which HMF, glucose and lignin have been exemplified as promising representatives. The long-standing benefits as well as existing limitations of reviewed designed strategies have been presented in **Table 1**. In addition, **Table S2** concretely summarizes how specific design strategy improves the performance of the investigated hybrid water electrolysis systems, in terms of reduced cell voltage, enhanced H₂ production efficiency, and simultaneous access to value-added products. In spite of the progress achieved, bridging the current-generation hybrid water electrolysis systems to the future-advanced ones still require more efforts. Hence, the following section highlights the current research challenges, as well as pioneering examples of emerging strategies for developing the next generation of robust hybrid water electrolysis systems.

(i) Multiple design strategies for advanced 2D nanomaterials: To date, single design strategies have been widely employed for 2D nanomaterials modification, targeting the promoted activity, selectivity or durability, respectively. To comprehensively improve the catalytic performance of developed 2D nanomaterials, employing multiple design strategies on one material is considered to be a more versatile technique. Here, we have summarized the

complementation of reviewed design strategies (**Table 1**) to guide smarter and more efficient 2D nanomaterial design. In addition, selective design strategies for anode and cathode material should be applied in a compatible manner so as to boost biomass valorization as well as H₂ production simultaneously, while bifunctional design strategies are highly desired to simplify the material fabrication and avoid cross-contamination under oxidative/reductive conditions.

(ii) Comprehensive investigation of catalyst interfaces under operation: It is well known that catalyst interfaces play an important role in governing the catalytic performance in terms of reactivity, selectivity and stability. In this context, a clear understanding of catalyst interfacial processes such as dynamic chemical/structural/electronic evolution, formation/interaction of key electroactive intermediates, and dominant reaction pathways, is required to rationalize the selection of design strategies and to drive the knowledge-based development of next-generation biomass valorization/HER electrocatalysts.

Combination of (photo-)electrochemical and cutting-edge *in situ* characterization techniques under operation can offer valuable insights at atomic- and molecular- levels to this end, leading to emergence of a wide range of *in situ* microscopic and spectroscopic methods, such as surface interrogation-scanning electrochemical microscopy (SI-SECM) for quantitative information of surface adsorbates,[122-124] transmission electron microscopy (TEM) for dynamic structural and morphological evolution at nano- / atomic-scale,[125] Fourier transform infrared spectroscopy (FTIR)[64, 126, 127] and Raman spectroscopy[128-131] for delivering structural information on surface-formed species, surface-bound adsorbates and species in the electrochemical double-layer, vibrational sum-frequency generation (vSFG) for accessing the structure of water molecules at the catalyst/water interface without bulk signal contribution,[132-134] X-ray absorption spectroscopy (XAS) for capturing the transformations of the local chemistry of the probed element, e.g., precise information on electronic structure, bond length, oxidation state, and the coordination environment under operation,[135-138] X-ray diffraction (XRD) for tracking crystal structure and phase transitions,[139, 140] and X-ray photoelectron spectroscopy (XPS) for surface elemental composition and oxidation states alteration under operation.[141, 142]

In addition to these landmarks, facilitating the use of machine-learning methods for theoretical calculation is versatile approach for in-depth kinetic modeling of the focused catalyst interfaces, which can be used to predict the reaction mechanism by calculating the energy levels of the electrons in the catalytic material and the interactions between the electrons and the ions in the electrolyte.[143-146]

Table 1. A summary of the benefits, limitations and complementation of the reviewed design strategies in biomass valorization coupled with H_2 production.

Design strategies	Benefits	Limitations	Complementary strategies
Host Structure Remodeling[147-152]			
Heteroatom doping	• Enhance catalytic activity • Tailor electronic properties and surface chemistry	• Difficult to control the distribution of heteroatoms uniformly • Complex synthesis processes	• **Surface engineering and Integration of 2D nanomaterials into 3D matrixes:** Ensure uniform dispersion of doped heteroatom • **Defect/vacancy engineering:** Simplify the synthesis process as defect/vacancy sites can facilitate the incorporation of heteroatoms
Defect/vacancy engineering	• Create more active sites • Improve reaction kinetics	• Excessive defects may compromise structural integrity • Difficult to control defect density	• **Heteroatom doping:** Mitigate the risk of compromising integrity by stabilizing the structure • **Construction of heterostructures:** Reduce the impact of excessive defects by providing additional mechanical support • **Surface engineering:** Maintain the uniformity of defect density by functionalizing the surface with specific properties
Co-catalysts engineering	• Enable synergistic effects with the host material • Enhance selectivity and efficiency	• Possible leaching of Co-catalysts • Higher cost due to multiple components • Complexity of selection and integration of suitable Co-catalysts	• **Heteroatom doping and Defect/vacancy engineering**: Reduce the risk of leaching by creating more robust active sites • **Construction of heterostructures**: Simplify the integration process by providing a more stable structure • **Integration of 2D nanomaterials into 3D matrixes:** Address the complexity of selection and integration by providing a more stable structure

ARTICLE   Journal Name

Structure Assembly Design[38, 153-157]

|			
Construction of heterostructures	• Enhance charge separation • Improve catalytic performance • Synergistic effects between different components	• Complex fabrication • Potential stability issues under reaction conditions	• **Surface engineering:** Achieve uniform integration and simplify the fabrication process • **Heteroatom doping and defect/vacancy engineering**: Address stability issues by improving the interaction between different components • **Integration of 2D nanomaterials into 3D matrixes**: Increase stability by improving the mechanical stability
Surface engineering	• Improve catalytic selectivity • Increase surface area • Enhance interaction with reactants	• Require precise control • Potential for surface contamination • Ununiformed surface coverage	• **Heteroatom doping and defect/vacancy engineering**: Achieve uniform surface coverage and reduce contamination by stabilizing functional groups as anchoring points and improving the interaction with reactants • **Construction of heterostructures and integration of 2D nanomaterials into 3D matrixes**: Reduce the risk of contamination and improve uniform surface coverage
Integration of 2D nanomaterials into 3D matrices	• High surface area • Unique electronic properties • Enable efficient charge transport and mass transfer	• Instable immobilization • Potential aggregation issues • Ununiformed dispersion and alignment of 2D materials in a 3D matrix	• **Construction of heterostructures and surface engineering:** Facilitate better immobilization and reducing aggregation by improving the interaction ability • **Heteroatom doping and defect/vacancy engineering:** Achieve uniform dispersion and reduce aggregation by introducing more reactive sites on the 2D nanomaterials • **Co-catalysts:** Improving alignment within the 3D matrixes by synergistic effect with the 2D nanomaterials

(iii) (Photo-)electrocatalyst recycling and regeneration: Under harsh catalytic conditions, the degradation of catalytic performance in terms of activity, selectivity and durability, is always difficult to predict and/or prevent. Even, the improper handling of the deactivated (photo-)electrocatalysts has caused serious implications, including waste generation and resource depletion.[158] To this end, reactive elements recycling, as well as sustained performance regeneration of the aging catalyst are essential for environmental and economic relevance, which is however limited by not only high cost, but also high energy consumption.[159-162] Notably, the lifespan of 2D nanomaterial-based (photo-)electrocatalysts can be extended in more eco-friendly modes,[163, 164] like employing green synthesis method (*e.g.* grinding, milling, and laser-assisted methods) or electrochemical activation approach. More remarkably, to re-attain superior performance, they can be re-modified by considerate design strategies[165] summarized in this review.

(iv) Strategical bridging the lab-scale to industrial-scale: Despite significant progress in the design and fabrication of highly efficient 2D nanomaterials, there is still a gap between laboratory scale and industrial scale for advanced biomass valorization coupled with H_2 production.[166, 167] On one hand, low-cost manufacturing and scaling up approaches of 2D nanomaterials should be developed to this

end.[168] As an instructive example, roll-to-roll chemical vapor deposition (CVD) reactors are emerging as prominent tool to produce continuous and uniform films of 2D nanomaterials on various substrates (*e.g.* steel sheet, titanium sheet, and carbon foam) for industrial demands.[169] On the other hand, integration of the obtained cost-efficient and activity-intensive 2D nanomaterial into suitable electrolyzer is considered to be another wise strategy to meet industrial demands. In this regard, flow electrolyzer shows enormous potentials for the continuous production of H_2 and valuable chemicals, benefitting from a number of significant advantages over batch cell including: (1) higher productivity and yield, (2) better control and optimization of the reaction parameters, (3) easier separation and purification of the products, and (4) lower energy consumption and waste generation.[170] More promisingly, employment of several flow electrolyzers in a row will offer a great opportunity to improve the efficiency, selectivity, and scalability of targeting reactions.

Considering the aforementioned challenges and emerging solutions, a schematic representation of the four-gear concept is depicted in **Figure 8**, demonstrating how the four interrelated, yet independent parts can form a whole.
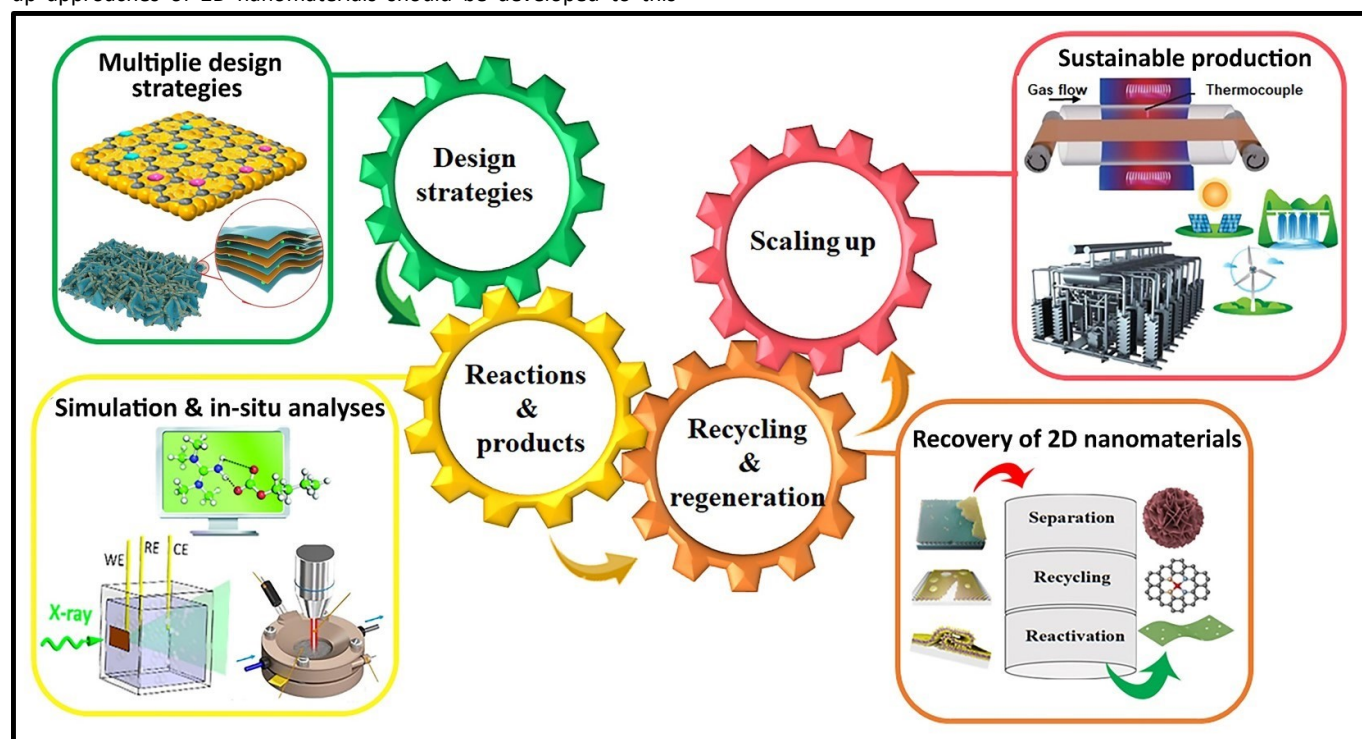
Fig. 8. A schematic representation of current challenges and suggested solutions.

4. Conclusion

In summary, this review highlights the design and application of versatile 2D nanomaterials in hybrid water electrolysis technology, which is able to simultaneously produce green H_2 fuels and valuable

chemicals/intermediates from naturally abundant biomass feedstocks. Specifically, this review provides a comprehensive summary of recently-developed design strategies (incl. benefits, limitations and complementation) for functional nanostructured 2D (photo-)electrocatalysts for HMFOR, GOR or LOR coupled with HER. A thorough literature survey reveals that, benefiting from rational

design strategies, the enhanced physical and chemical properties of 2D nanomaterials largely facilitate hybrid water electrolysis performance. Notably, it is crucial to address the current challenges related to intelligent design toward next-generation 2D nanostructured electrocatalysts, insightful (photo-)electrochemical surface investigation over catalysis, sustainable recovery and regeneration of active species after service, as well as and industrial-relevance scaling-up applications. Addressing these practical issues provides a great opportunity to advance hybrid water (photo-)electrolysis technology towards higher efficiency and lower cost.

Author Contributions

B.F.M. and D.G. conceived the idea for the review. The manuscript was written and reviewed through contributions of all authors. All authors have given approval to the final version of the manuscript.

Conflicts of interest

The authors declare no conflict of interests.

Data availability

This review article does not present any new data analyzed by the authors. All data discussed in this review are derived from previously published studies with respective citation in the text. Additional supporting data and comparison table have been included, which are cited accordingly within the Electronic Supplementary Information (ESI).

Acknowledgements

Notes and references

1. M. Faraji, M. Yousefi, S. Yousefzadeh, M. Zirak, N. Naseri, T. H. Jeon, W. Choi and A. Z. Moshfegh, *Energy Envior. Sci.*, 2019, **12**, 59-95.
2. Y. S. Park, J. Yang, J. Lee, M. J. Jang, J. Jeong, W.-S. Choi, Y. Kim, Y. Yin, M. H. Seo and Z. Chen, *Appl. Catal. B*, 2020, **278**, 119276.
3. N.-T. Suen, S.-F. Hung, Q. Quan, N. Zhang, Y.-J. Xu and H. M. Chen, *Chem Soc Rev*, 2017, **46**, 337-365.
4. S. Anantharaj, S. R. Ede, K. Sakthikumar, K. Karthick, S. Mishra and S. Kundu, *Acs Catalysis*, 2016, **6**, 8069-8097.
5. A. Raveendran, M. Chandran and R. Dhanusuraman, *RSC advances*, 2023, **13**, 3843-3876.
6. J. E. Lee, K.-J. Jeon, P. L. Show, S.-C. Jung, Y. J. Choi, G. H. Rhee, K.-Y. A. Lin and Y.-K. Park, *Fuel*, 2022, **308**, 122048.
7. L. Wang, Y. Tong, J. Feng, J. Hou, J. Li, X. Hou and J. Liang, *Sustain Mater. Techno.*, 2019, **19**, e00089.
8. X. Li, R. Shen, S. Ma, X. Chen and J. Xie, *Appl. Surf. Sci.*, 2018, **430**, 53-107.
9. J. Yi, W. El-Alami, Y. Song, H. Li, P. M. Ajayan and H. Xu, *Chemical Engineering Journal*, 2020, **382**, 122812.
10. H. Zhou, F. Yu, Q. Zhu, J. Sun, F. Qin, L. Yu, J. Bao, Y. Yu, S. Chen and Z. Ren, *Energy Envior. Sci.*, 2018, **11**, 2858-2864.
11. T. Naito, T. Shinagawa, T. Nishimoto and K. Takanabe, *Inorg. Chem. Front.*, 2021, **8**, 2900-2917.
12. C. C. L. McCrory, S. Jung, J. C. Peters and T. F. Jaramillo, *J. Am. Chem. Soc*, 2013, **135**, 16977-16987.
13. X. Xie, L. Du, L. Yan, S. Park, Y. Qiu, J. Sokolowski, W. Wang and Y. Shao, *Advanced Functional Materials*, 2022, **32**, 2110036.
14. X. Liu, Y. Ji, G. Chen, X. Peng, L. Yi, J. Chen, X. Feng and Z. Wen, *Small Structures*, 2021, **2**, 2100121.
15. B. You, X. Liu, X. Liu and Y. Sun, *ACS Catal.*, 2017, **7**, 4564-4570.
16. K. Xiang, D. Wu, X. Deng, M. Li, S. Chen, P. Hao, X. Guo, J. L. Luo and X. Z. Fu, *Adv. Funct. Mater.*, 2020, **30**, 1909610.
17. W.-J. Liu, L. Dang, Z. Xu, H.-Q. Yu, S. Jin and G. W. Huber, *ACS Catal.*, 2018, **8**, 5533-5541.
18. B. You, X. Liu, N. Jiang and Y. Sun, *J. Am. Chem. Soc*, 2016, **138**, 13639-13646.
19. C. Lamy, A. Devadas, M. Simoes and C. Coutanceau, *Electrochim. Acta*, 2012, **60**, 112-120.
20. W. Guo, L. Li, L. Li, S. Tian, S. Liu and Y. Wu, *Int. J. Hydrogen Energy.*, 2011, **36**, 9415-9419.
21. Y. Huang, X. Chong, C. Liu, Y. Liang and B. Zhang, *Angew. Chem., Int. Ed.*, 2018, **130**, 13347-13350.
22. S. Xue, S. Watzele, V. Čolić, K. Brandl, B. Garlyyev and A. S. Bandarenka, *ChemSusChem*, 2017, **10**, 4812-4816.
23. W. Peng, L. Xiao, B. Huang, L. Zhuang and J. Lu, *J. Phys. Chem. C*, 2011, **115**, 23050-23056.
24. J. Huang, J. Cai and J. Wang, *ACS Appl. Energy Mater.*, 2020, **3**, 4108-4113.
25. J. Y. Zhang, H. Wang, Y. Tian, Y. Yan, Q. Xue, T. He, H. Liu, C. Wang, Y. Chen and B. Y. Xia, *Angew. Chem., Int. Ed.*, 2018, **57**, 7649-7653.
26. P. Babar, A. Lokhande, V. Karade, I. J. Lee, D. Lee, S. Pawar and J. H. Kim, *J. Colloid Interface Sci.*, 2019, **557**, 10-17.
27. X. Zhao, L. Dai, Q. Qin, F. Pei, C. Hu and N. Zheng, *Small*, 2017, **13**, 1602970.
28. J. Zheng, X. Chen, X. Zhong, S. Li, T. Liu, G. Zhuang, X. Li, S. Deng, D. Mei and J. G. Wang, *Adv. Funct. Mater.*, 2017, **27**, 1704169.
29. Z. Fan, W. Zhang, L. Li, Y. Wang, Y. Zou, S. Wang and Z. Chen, *Green Chem.*, 2022, **24**, 7818-7868.
30. H. Luo, J. Barrio, N. Sunny, A. Li, L. Steier, N. Shah, I. E. Stephens and M. M. Titirici, *Adv. Energy Mater."*, 2021, **11**, 2101180.
31. Z. Sun, B. Fridrich, A. De Santi, S. Elangovan and K. Barta, *Chem. Rev.*, 2018, **118**, 614-678.
32. C. Liu, S. Wu, H. Zhang and R. Xiao, *Fuel Process. Technol.*, 2019, **191**, 181-201.
33. M.-I. Jamesh and X. Sun, *J. Power Sources*, 2018, **400**, 31-68.

Sustainable Energy & Fuels Accepted Manuscript

ARTICLE

34. C. Deng, C. Y. Toe, X. Li, J. Tan, H. Yang, Q. Hu and C. He, *Adv. Energy Mater.*", 2022, 2201047.

35. S. Bellani, A. Bartolotta, A. Agresti, G. Calogero, G. Grancini, A. Di Carlo, E. Kymakis and F. Bonaccorso, *Chem Soc Rev*, 2021.

36. D. Scarano and F. Cesano, *Mater.*, 2021, **14**, 7108.

37. C. S. Bongu, S. Tasleem, M. R. Krishnan and E. H. Alsharaeh, *Sustainable Energy & Fuels*, 2024, DOI: 10.1039/D4SE00497C.

38. H. He, L. Guan and H. Le Ferrand, *J. Mater. Chem. A*, 2022.

39. M. H. Kalantari and X. Zhang, *Nanomater.*, 2022, **13**, 117.

40. B. Zheng, S. Yu, Z. Chen and Y.-X. Huo, *Front. microbiol.*, 2022, **13**, 933882.

41. A. Zhang, Y. Liang, H. Zhang, Z. Geng and J. Zeng, *Chem Soc Rev*, 2021.

42. H. Zhu, X. Gan, A. McCreary, R. Lv, Z. Lin and M. Terrones, *Nano Today*, 2020, **30**, 100829.

43. J. Xie, J. Zhang, S. Li, F. Grote, X. Zhang, H. Zhang, R. Wang, Y. Lei, B. Pan and Y. Xie, *J. Am. Chem. Soc*, 2013, **135**, 17881-17888.

44. Z. Ning, S. Gan, H. Xu, C. Gu, P. Zhu, J. Zhou and G. Xiao, *J. Mater. Chem. A*, 2024, **12**, 5885-5897.

45. M. Gao, L. Zhu, C. K. Peh and G. W. Ho, *Energy Envior. Sci.*, 2019, **12**, 841-864.

46. J. Li and N. Wu, *Catal. Sci. Technol.*, 2015, **5**, 1360-1384.

47. D. N. Tafen, J. Wang, N. Wu and J. P. Lewis, *Appl. Phys. Lett.*, 2009, **94**, 093101.

48. H. P. Maruska and A. K. Ghosh, *Sol. Energy Mater.*, 1979, **1**, 237-247.

49. J. M. Luther, P. K. Jain, T. Ewers and A. P. Alivisatos, *Nat. Mater.*, 2011, **10**, 361-366.

50. T. Wei, W. Liu, S. Zhang, Q. Liu, J. Luo and X. Liu, *ChemComm*, 2023, **59**, 442-445.

51. J. Zhang, P. Yu, G. Zeng, F. Bao, Y. Yuan and H. Huang, *J. Mater. Chem. A*, 2021, **9**, 9685-9691.

52. D. Li, Y. Huang, Z. Li, L. Zhong, C. Liu and X. Peng, *J. Chem. Eng.*, 2022, **430**, 132783.

53. D. Li, Z. Li, R. Zou, G. Shi, Y. Huang, W. Yang, W. Yang, C. Liu and X. Peng, *Appl. Catal. B*, 2022, **307**, 121170.

54. T. Cui, L. Ma, S. Wang, C. Ye, X. Liang, Z. Zhang, G. Meng, L. Zheng, H.-S. Hu and J. Zhang, *J. Am. Chem. Soc*, 2021, **143**, 9429-9439.

55. X. Hao, Y. Quansheng, S. Dan, Y. Honghui, L. Jidong, F. Jiangtao and Y. Wei, *J. Hazard. Mater.*, 2015, **286**, 509-516.

56. C. Zhao, Z. Li, T. Fan, C. Xiao and Y. Xie, *Research*, 2020, **2020**.

57. X. Yan, L. Zhuang, Z. Zhu and X. Yao, *Nanoscale*, 2021, **13**, 3327-3345.

58. T. Tang, Z. Wang and J. Guan, *CHINESE J CATAL*, 2022, **43**, 636-678.

59. D. Maarisetty and S. S. Baral, *J. Mater. Chem. A*, 2020, **8**, 18560-18604.

60. J. Yan, G. Wu, N. Guan, L. Li, Z. Li and X. Cao, *Phys. Chem. Chem. Phys.*, 2013, **15**, 10978-10988.

61. M. Xu, X. Ruan, D. Meng, G. Fang, D. Jiao, S. Zhao, Z. Liu, Z. Jiang, K. Ba, T. Xie, W. Zhang, J. Leng, S. Jin, S. K. Ravi and X. Cui, *Adv. Funct. Mater.*, **n/a**, 2402330.

62. B. Zhang, Z. Yang, C. Yan, Z. Xue and T. Mu, *Small*, 2023, **19**, 2207236.

63. B. Zhu, Y. Qin, J. Du, F. Zhang and X. Lei, *ACS Sustain Chem Eng*, 2021, **9**, 11790-11797.

64. Z. Tian, Y. Da, M. Wang, X. Dou, X. Cui, J. Chen, R. Jiang, S. Xi, B. Cui and Y. Luo, *Nat. Commun.*, 2023, **14**, 142.

65. J. Yang, D. Wang, H. Han and C. Li, *Acc. Chem. Res.*, 2013, **46**, 1900-1909.

66. M. Kumar, B. Meena, P. Subramanyam, D. Suryakala and C. Subrahmanyam, *NPG Asia Mater.*, 2022, **14**, 88.

67. X. T. Xu, L. Pan, X. Zhang, L. Wang and J. J. Zou, *Adv. Sci.*, 2019, **6**, 1801505.

68. H. Wang, L. Zhang, Z. Chen, J. Hu, S. Li, Z. Wang, J. Liu and X. Wang, *Chem Soc Rev*, 2014, **43**, 5234-5244.

69. H. Hou, X. Zeng and X. Zhang, *Sci. China Mater.*, 2020, **63**, 2119-2152.

70. S. Liang, L. Pan, T. Thomas, B. Zhu, C. Chen, J. Zhang, H. Shen, J. Liu and M. Yang, *J. Chem. Eng.*, 2021, **415**, 128864.

71. S. Wang, X. Gao, X. Hang, X. Zhu, H. Han, X. Li, W. Liao and W. Chen, *J. Am. Chem. Soc*, 2018, **140**, 6271-6277.

72. D. Rauber, T. K. Dier, D. A. Volmer and R. Hempelmann, *ZPC*, 2018, **232**, 189-208.

73. J. Miao, Y. Ma, X. Wang, Y. Li, H. Wang, L. Zhang, J. Zhang, Y. Qin and J. Gao, *Appl. Catal. B*, 2023, 122937.

74. H. Wang, W. Fu, X. Yang, Z. Huang, J. Li, H. Zhang and Y. Wang, *J. Mater. Chem. A*, 2020, **8**, 6926-6956.

75. X. Ruan, S. Li, C. Huang, W. Zheng, X. Cui and S. K. Ravi, *Adv. Mater.*, 2024, **36**, 2305285.

76. P. Solís-Fernández, M. Bissett and H. Ago, *Chem Soc Rev*, 2017, **46**, 4572-4613.

77. X. Du, J. Huang, J. Zhang, Y. Yan, C. Wu, Y. Hu, C. Yan, T. Lei, W. Chen and C. Fan, *Angew. Chem., Int. Ed.*, 2019, **58**, 4484-4502.

78. X. Wu, Y. Wang and Z.-S. Wu, *Chem.*, 2022.

79. J. Low, S. Cao, J. Yu and S. Wageh, *ChemComm*, 2014, **50**, 10768-10777.

80. J. Su, G. D. Li, X. H. Li and J. S. Chen, *Adv. Sci.*, 2019, **6**, 1801702.

81. X. Li and J. Wang, *InfoMat*, 2020, **2**, 3-32.

82. Q. Wei, F. Xiong, S. Tan, L. Huang, E. H. Lan, B. Dunn and L. Mai, *Adv. Mater.*, 2017, **29**, 1602300.

83. Y. Li, M. Ma, D. Yi, Q. Zhou, J. Chen, Y. Bian, W. Niu, C. Yang, Z. Yin, Z. Wang and A. Tang, *Adv. Funct. Mater.*, **n/a**, 2407271.

84. L. Zhang, J. Zhang, H. Yu and J. Yu, *Adv. Mater.*, 2022, **34**, 2107668.

85. Q. Xu, L. Zhang, B. Cheng, J. Fan and J. Yu, *Chem.*, 2020, **6**, 1543-1559.

86. M. Sun, J. Yang, J. Huang, Y. Wang, X. Liu, Y. Qi and L. Zhang, *Langmuir*, 2023, **39**, 3762-3769.

87. Y. Zhong, R.-Q. Ren, J.-B. Wang, Y.-Y. Peng, Q. Li and Y.-M. Fan, *Catal. Sci. Technol.*, 2022, **12**, 201-211.

88. X. Deng, X. Kang, M. Li, K. Xiang, C. Wang, Z. Guo, J. Zhang, X.-Z. Fu and J.-L. Luo, *J. Mater. Chem. A*, 2020, **8**, 1138-1146.

89. F. Sun, Y. Zhou, Z. You, H. Xia, Y. Tuo, S. Wang, C. Jia and J. Zhang, *Small*, 2021, **17**, 2103307.

90. F. Bateni, M. NaderiNasrabadi, R. Ghahremani and J. A. Staser, *J. Electrochem. Soc.*, 2019, **166**, F1037.

91. M. NaderiNasrabadi, F. Bateni, Z. Chen, P. B. Harrington and J. A. Staser, *J. Electrochem. Soc.*, 2019, **166**, E317.

92. Y. Hu, H. Huang, J. Feng, W. Wang, H. Guan, Z. Li and Z. Zou, *Solar RRL*, 2021, **5**, 2100100.

93. F. E. Osterloh, *Chem Soc Rev*, 2013, **42**, 2294-2320.

Sustainable Energy & Fuels Accepted Manuscript

94. Y. Zhou, L. Zhang, L. Lin, B. R. Wygant, Y. Liu, Y. Zhu, Y. Zheng, C. B. Mullins, Y. Zhao and X. Zhang, *Nano Lett.*, 2017, **17**, 8012-8017.

95. M. Bae, Y. Kang, D. W. Lee, D. Jeon and J. Ryu, *Adv. Energy Mater."*, 2022, **12**, 2201452.

96. X. Deng, M. Li, Y. Fan, L. Wang, X.-Z. Fu and J.-L. Luo, *Appl. Catal. B*, 2020, **278**, 119339.

97. C. Sun, D. Zhang, Y. Zhao, C. Song and D. Wang, *COLL SURF A COLLOID SURF A PHYSICOCHEM ENG*, 2022, **650**, 129597.

98. Z. Zhou, C. Chen, M. Gao, B. Xia and J. Zhang, *Green Chem.*, 2019, **21**, 6699-6706.

99. Y. Wang, W. Yan, M. Ni, C. Zhu and H. Du, *ChemComm*, 2023, **59**, 2485-2488.

100. R. Ghahremani, F. Farales, F. Bateni and J. A. Staser, *J. Electrochem. Soc.*, 2020, **167**, 043502.

101. K. Jakubow-Piotrowska, B. Witkowski and J. Augustynski, *Commun. Chem.*, 2022, **5**, 125.

102. Y. Xue, G. Zhao, R. Yang, F. Chu, J. Chen, L. Wang and X. Huang, *Nanoscale*, 2021, **13**, 3911-3936.

103. L. P. Lefebvre, J. Banhart and D. C. Dunand, *Adv. Eng. Mater.*, 2008, **10**, 775-787.

104. W. Zhu, R. Zhang, F. Qu, A. M. Asiri and X. Sun, *ChemCatChem*, 2017, **9**, 1721-1743.

105. C. Körner and R. F. Singer, *Adv. Eng. Mater.*, 2000, **2**, 159-165.

106. D. Gao, R. Liu, S. Liu, S. Greiner, M. Anjass, J. Biskupek, U. Kaiser, H. Braun, T. Jacob and C. Streb, *ACS Appl. Mater. Interfaces.*, 2021, **13**, 19048-19054.

107. D. Gao, R. Liu, J. Biskupek, U. Kaiser, Y. F. Song and C. Streb, *Angew. Chem., Int. Ed.*, 2019, **58**, 4644-4648.

108. F. Chen, C. Chen, Q. Hu, B. Xiang, T. Song, X. Zou, W. Li, B. Xiong and M. Deng, *J. Chem. Eng.*, 2020, **401**, 126145.

109. R. Zhang, J. Liu, H. Guo and X. Tong, *Mater. Lett.*, 2015, **139**, 55-58.

110. D. Gao, S. Liu, R. Liu and C. Streb, *Chem. Eur. J.*, 2020, **26**, 11109-11112.

111. C. Chen, Z. Zhou, J. Liu, B. Zhu, H. Hu, Y. Yang, G. Chen, M. Gao and J. Zhang, *Appl. Catal. B*, 2022, **307**, 121209.

112. Y. Xie, L. Sun, X. Pan, Z. Zhou and G. Zhao, *Appl. Catal. B*, 2023, **338**, 123068.

113. Y. Xin, F. Wang, L. Chen, Y. Li and K. Shen, *Green Chem.*, 2022, **24**, 6544-6555.

114. W.-J. Liu, Z. Xu, D. Zhao, X.-Q. Pan, H.-C. Li, X. Hu, Z.-Y. Fan, W.-K. Wang, G.-H. Zhao, S. Jin, G. W. Huber and H.-Q. Yu, *Nat. Commun.*, 2020, **11**, 265.

115. N. Wang, R. Xue, N. Yang, H. Sun, B. Zhang, Z. Ma, Y. Ma and L. Zang, *J. Alloys Compd.*, 2022, **929**, 167324.

116. M. Garedew, F. Lin, B. Song, T. M. DeWinter, J. E. Jackson, C. M. Saffron, C. H. Lam and P. T. Anastas, *ChemSusChem*, 2020, **13**, 4214-4237.

117. M. Zirbes, D. Schmitt, N. Beiser, D. Pitton, T. Hoffmann and S. R. Waldvogel, *ChemElectroChem*, 2019, **6**, 155-161.

118. Z. Fang, J. E. Jackson and E. L. Hegg, *ACS Sustain Chem Eng*, 2022, **10**, 7545-7552.

119. D. Schmitt, C. Regenbrecht, M. Hartmer, F. Stecker and S. R. Waldvogel, *Beilstein J. Org. Chem.*, 2015, **11**, 473-480.

120. D. Schmitt, C. Regenbrecht, M. Schubert, D. Schollmeyer and S. R. Waldvogel, *Holzforschung*, 2017, **71**, 35-41.

121. M. Breiner, M. Zirbes and S. R. Waldvogel, *Green Chem.*, 2021, **23**, 6449-6455.

122. Y. Wu and N. Liu, *Chem.*, 2018, **4**, 438-465.

123. K. Zhu, X. Zhu and W. Yang, *Angew. Chem., Int. Ed.*, 2019, **58**, 1252-1265.

124. A. Preet and T.-E. Lin, *Catalysts*, 2021, **11**, 594.

125. N. Ortiz Peña, D. Ihiawakrim, M. Han, B. Lassalle-Kaiser, S. Carenco, C. Sanchez, C. Laberty-Robert, D. Portehault and O. Ersen, *ACS nano*, 2019, **13**, 11372-11381.

126. P. Su, V. Prabhakaran, G. E. Johnson and J. Laskin, *Anal. Chem.*, 2018, **90**, 10935-10942.

127. T. Faverge, B. Gilles, A. Bonnefont, F. Maillard, C. Coutanceau and M. Chatenet, *ACS Catal.*, 2023, **13**, 2657-2669.

128. D.-J. Chen and Y. Tong, *ChemComm*, 2015, **51**, 5683-5686.

129. S.-i. Ogino, T. Itoh, D. Mabuchi, K. Yokoyama, K. Motomiya, K. Tohji and Y. Sato, *J. Phys. Chem. C*, 2016, **120**, 7133-7143.

130. Y.-H. Wang, S. Li, R.-Y. Zhou, S. Zheng, Y.-J. Zhang, J.-C. Dong, Z.-L. Yang, F. Pan, Z.-Q. Tian and J.-F. Li, *Nat. Protoc.*, 2023, **18**, 883-901.

131. D. Chen, Y. Ding, X. Cao, L. Wang, H. Lee, G. Lin, W. Li, G. Ding and L. Sun, *Angew. Chem., Int. Ed.*, 2023, **62**, e202309478.

132. N. Zhang, Y. Zou, L. Tao, W. Chen, L. Zhou, Z. Liu, B. Zhou, G. Huang, H. Lin and S. Wang, *Angew. Chem., Int. Ed.*, 2019, **131**, 16042-16050.

133. R. De and B. Dietzek-Ivanšić, *Chem. Eur. J.*, 2022, **28**, e202200407.

134. A. Kemna, N. García Rey and B. Braunschweig, *ACS Catal.*, 2019, **9**, 6284-6292.

135. J. Timoshenko and B. Roldan Cuenya, *Chem. Rev.*, 2020, **121**, 882-961.

136. M. Risch, D. M. Morales, J. Villalobos and D. Antipin, *Angew. Chem., Int. Ed.*, 2022, **61**, e202211949.

137. S. Chen, L. Ma, Z. Huang, G. Liang and C. Zhi, *Cell Rep. Phys. Sci.*, 2022, 100729.

138. N. Gupta, C. Segre, C. Nickel, C. Streb, D. Gao and K. D. Glusac, *ACS Appl. Mater. Interfaces.*, 2024, **16**, 35793-35804.

139. C.-J. Chang, Y. Zhu, J. Wang, H.-C. Chen, C.-W. Tung, Y.-C. Chu and H. M. Chen, *J. Mater. Chem. A*, 2020, **8**, 19079-19112.

140. Y. Zhu, T.-R. Kuo, Y.-H. Li, M.-Y. Qi, G. Chen, J. Wang, Y.-J. Xu and H. M. Chen, *Energy Envior. Sci.*, 2021, **14**, 1928-1958.

141. K. A. Stoerzinger, W. T. Hong, E. J. Crumlin, H. Bluhm and Y. Shao-Horn, *Acc. Chem. Res.*, 2015, **48**, 2976-2983.

142. Y.-D. Cao, W.-X. Mu, M. Gong, L.-L. Fan, J. Han, H. Liu, B. Qi and G.-G. Gao, *Dalton Trans.*, 2023.

143. J. K. Nørskov, F. Abild-Pedersen, F. Studt and T. Bligaard, *Proc. Natl. Acad. Sci.*, 2011, **108**, 937-943.

144. Y.-K. Lee, *Journal*, 2021, **11**, 454.

145. Z. W. Seh, J. Kibsgaard, C. F. Dickens, I. Chorkendorff, J. K. Nørskov and T. F. Jaramillo, *Sci.*, 2017, **355**, eaad4998.

146. L. Ostervold, S. I. P. Bakovic, J. Hestekin and L. F. Greenlee, *RSC Adv.*, 2021, **11**, 31208-31218.

147. X. Wang, G. Sun, P. Routh, D.-H. Kim, W. Huang and P. Chen, *Chem Soc Rev*, 2014, **43**, 7067-7098.

148. B. F. Mohazzab, A. Akhundi, K. Rahimi, B. Jaleh and A. Z. Moshfegh, *ACS Appl. Energy Mater.*, 2022, **5**, 12283-12296.

149. S. Mansoor, M. Tayyab, M. Khan, Z. Akmal, L. Zhou, J. Lei, M. Anpo and J. Zhang, *Research on Chemical Intermediates*, 2023, **49**, 3723-3745.

150. A. Kumar, P. Raizada, A. Hosseini-Bandegharaei, V. K. Thakur, V.-H. Nguyen and P. Singh, *J. Mater. Chem. A*, 2021, **9**, 111-153.

151. V. Gurylev and V. Gurylev, *Nanostructured Photocatalyst via Defect Engineering: Basic Knowledge and Recent Advances*, 2021, 37-72.

152. H. L. Chia, C. C. Mayorga-Martinez and M. Pumera, *Adv. Funct. Mater.*, 2021, **31**, 2102555.

153. H. Zheng, Y. Li, H. Liu, X. Yin and Y. Li, *Chem Soc Rev*, 2011, **40**, 4506-4524.

154. X. Sun, L. Shi, H. Huang, X. Song and T. Ma, *ChemComm*, 2020, **56**, 11000-11013.

155. L. Maggini and R. R. Ferreira, *J. Mater. Chem. C*, 2021, **9**, 15721-15734.

156. B. Ikenson, *Scilight*, 2022, **2022**.

157. C. Feng, Z.-P. Wu, K.-W. Huang, J. Ye and H. Zhang, *Adv. Mater.*, 2022, **34**, 2200180.

158. M. G. Kibria, N. I. Masuk, R. Safayet, H. Q. Nguyen and M. Mourshed, *INT J ENVIRON RES*, 2023, **17**, 20.

159. S. Cheng, L. Wei, X. Zhao and J. Julson, *Catalysts*, 2016, **6**, 195.

160. I. V. Yentekakis and F. Dong, *Front. Environ. Chem.*, 2020, 5.

161. C. H. Bartholomew and M. D. Argyle, *Journal*, 2015, **5**, 949-954.

162. X. Zhang, S. Xu, J. Tang, L. Fu and H. Karimi-Maleh, *Catalysts*, 2022, **12**, 818.

163. L. X. Chen, Z. W. Chen, M. Jiang, Z. Lu, C. Gao, G. Cai and C. V. Singh, *J. Mater. Chem. A*, 2021, **9**, 2018-2042.

164. K. Khan, A. K. Tareen, M. Aslam, R. U. R. Sagar, B. Zhang, W. Huang, A. Mahmood, N. Mahmood, K. Khan and H. Zhang, *Nano-Micro Letters*, 2020, **12**, 1-77.

165. N. Rohaizad, C. C. Mayorga-Martinez, M. Fojtů, N. M. Latiff and M. Pumera, *Chem Soc Rev*, 2021, **50**, 619-657.

166. H. Sun, X. Xu, H. Kim, W. Jung, W. Zhou and Z. Shao, *Energy Environ. Mater.*, 2022, e12441.

167. W. Li, H. Tian, L. Ma, Y. Wang, X. Liu and X. Gao, *Mater. Adv.*, 2022, **3**, 5598-5644.

168. S. H. Choi, S. J. Yun, Y. S. Won, C. S. Oh, S. M. Kim, K. K. Kim and Y. H. Lee, *Nat. Commun.*, 2022, **13**, 1484.

169. E. S. Polsen, D. Q. McNerny, B. Viswanath, S. W. Pattinson and A. John Hart, *Sci. Rep.*, 2015, **5**, 1-12.

170. D. Pollok and S. R. Waldvogel, *Chem. Sci.*, 2020, **11**, 12386-12400.

Design of nanostructured 2D (photo-)electrocatalysts for biomass valorization coupled with H₂ production

Bahareh Feizi Mohazzab,[*a] Kiarash Torabi,[b] and Dandan Gao[*a]

[a] Department of Chemistry, Johannes Gutenberg University Mainz, Duesbergweg 10-14, 55128 Mainz, Germany

Emails: bahareh.feizimohazzab@uni-mainz.de; dandan.gao@uni-mainz.de

[b] Department of Materials Engineering and Metallurgy, Faculty of Engineering,

Arak University, Arak 3815688349, Iran.

Data availability

This review article does not present any new data analyzed by the authors. All data discussed in this review are derived from previously published studies with respective citation in the text. Additional supporting data and comparison table have been included, which are cited accordingly within the Electronic Supplementary Information (ESI).